J. Fluid Mech. (2025), *vol.* 1025, A40, doi:10.1017/jfm.2025.10956

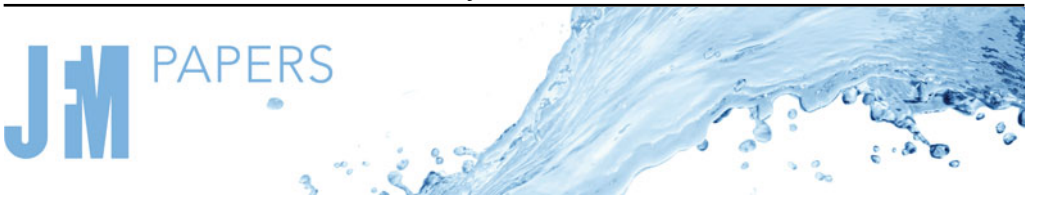

Weakly nonlinear analysis of particle-laden Rayleigh–Bénard convection

Thota Srinivas[1] **and Gaurav Tomar**[1]

[1]Department of Mechanical Engineering, Indian Institute of Science, Bengaluru 560012, India

Corresponding author: Gaurav Tomar, gtom@iisc.ac.in

(Received 28 March 2025; revised 12 November 2025; accepted 12 November 2025)

We investigate the effect of inertial particles on Rayleigh-Bénard convection using weakly nonlinear stability analysis. An Euler–Euler/two-fluid formulation is used to describe the flow instabilities in particle-laden Rayleigh–Bénard convection. The weakly nonlinear results are presented near the critical point (bifurcation point) for water droplets in the dry air system. We show that supercritical bifurcation is the only type of bifurcation beyond the critical point in particle-laden Rayleigh–Bénard convection. Interaction of settling particles with the flow and the Reynolds stress or distortion terms emerges due to the nonlinear self-interaction of fundamental modes breaking down the top–bottom symmetry of the secondary flow structures. In addition to the distortion functions, the nonlinear interaction of fundamental modes generates higher harmonics, leading to the tendency of preferential concentration of uniformly distributed particles, which is completely absent in the linear stability analysis. Further, we show that in the presence of thermal energy coupling between the fluid and particles, the difference between the horizontally averaged heat flux at the hot and cold surfaces is equal to the net sensible heat flux advected by the particles. The difference between the heat fluxes at hot and cold surfaces increases with an increase in particle concentration.

Key words: Bénard convection, Buoyancy-driven instability, particle/fluid flow

1. Introduction

Particle-laden flows are ubiquitous in nature and industries, such as in the dispersion of water droplets in atmospheric clouds (Shaw 2003; Abade, Grabowski & Pawlowska 2018), aerosols and dust particles in the atmosphere (Chandrakar *et al.* 2020), crystals settling in the Earth's magma chambers (Martin & Nokes 1988; Koyaguchi *et al.* 1990; Molina, Burgisser & Oppenheimer 2015), mixing fuel droplets in combustion chambers

(Huang *et al.* 2021; Cao *et al.* 2024), spray coating (Pendar & Páscoa 2021), ejection of solid particles and ash due to volcanic eruption (Schwaiger, Denlinger & Mastin 2012; Yarushina, Bercovici & Michaut 2015), dispersion of pollen grains (Helbig *et al.* 2004; Robichaud & Comtois 2021), and dynamics of phytoplankton in ocean waters (Squires & Yamazaki 1995; Ruiz, Macías & Peters 2004). Due to this broad spectrum of applications, particle-laden flows are of great interest to fluid dynamicists and geophysicists. Hence to get a comprehensive understanding of these flows, various experimental and numerical techniques have been proposed in the literature (Kiger & Lasheras 1997; Hwang & Eaton 2006; Zhong, Funfschilling & Ahlers 2009; Brandt & Coletti 2022; Srinivas & Tomar 2025).

Microphysical mechanisms of rain initiation involve three stages, namely: activation of droplets on cloud condensation nuclei (size of the order of 0.05 μm), increase in the droplet size by condensation (reaches a size of the order of 10 μm) and by coalescence (Beard & Ochs 1993). Generally, droplets of radius larger than 50 μm settle under gravity and continue to grow via collisions with droplets in their path to reach a raindrop size of the order of 80$-$100 μm. It has been shown that theoretically, droplets should take times of the order of hours to reach 50 μm in size, despite the actual observations showing merely 15–20 min. Using tangling clustering instability proposed by Elperin *et al.* (2013) for thermally stratified flow, Elperin *et al.* (2015) provided the explanation for rapid droplet growth from 1 μm to 40$-$50 μm within 15–20 min. Recently, Poydenot & Andreotti (2024) showed the formation of raindrops through the attractive van der Waals and electrostatic interactions. However, the formation of local particle clusters from their initially uniform distribution in a thermally stratified flow is not well understood. In the present study, we use Rayleigh–Bénard convection as the model for the thermally stratified flow. It should be mentioned that in this work, we only take into account the momentum and thermal interaction among the fluid and the particulate phases, ignoring phase change phenomena such as condensation and evaporation. Therefore, only qualitative inferences for droplet dynamics in clouds can be made from the present study. Nevertheless, the analysis presented in this work is useful for understanding atmospheric phenomena like dust storms and aerosol dispersion.

The effect of settling particles on a weakly turbulent Rayleigh–Bénard convection has been studied by Oresta & Prosperetti (2013). They showed that the mechanical coupling between the particles and fluid increases the Nusselt number with increasing particle size. However, thermal coupling between the fluid and particles tends to make the fluid temperature uniform and thus reduces the strength of the convection of the underlying fluid flow. They also reported an unusual kind of reverse one-way coupling in the sense that the underlying flow was affected more significantly than the settling particles. Later, Oresta, Fornarelli & Prosperetti (2014) reviewed the mathematical formulations and the numerical methods for the particle and bubble-laden Rayleigh–Bénard convection. To understand the settling of dense crystals in magma chambers and planetary scale magma oceans, Patočka *et al.* (2020) conducted a numerical study on the rate of settling of particles in a rectangular two-dimensional Rayleigh–Bénard convection with Rayleigh number up to 10^{12} and Prandtl number ranging from 10 to 50. Four distinct settling regimes, namely, stone-like, bi-linear, transitional and dust-like regimes, have been observed based on the ratio of particle terminal speed and flow root mean square velocity. Similarly, Srinivas & Tomar (2024) analysed the effect of particle size on the particle cloud patterns in Rayleigh–Bénard convection. However, in these studies, the coupling between the fluid and the particles is one-way, where the fluid flow field affects the particle trajectories while the effect of particles on the underlying flow is ignored. Recently, Denzel, Bragg & Richter

(2023) developed a stochastic model to predict the residence times of the particles in a turbulent Rayleigh–Bénard convection using Euler–Lagrange formulation.

A linear stability analysis of a fluid confined between more realistic rigid surfaces and heated from below was performed by Sir Harold Jeffreys (Jeffreys 1928). The critical Rayleigh number Ra_c and critical wavenumber k_c were obtained as 1708 and 3.117, respectively. However, we expect, based on various numerical and experimental studies (Hetsroni & Sokolov 1971; Sun & Faeth 1986; Gore & Crowe 1989; Lance, Marie & Bataille 1991), that the collective dynamics of small particles or bubbles can affect the underlying flow significantly. However, most of the studies have been performed for isothermal systems (Balachandar & Eaton 2010; Kuerten 2016; Maxey 2017). The effect of the suspended particles on the convective heat transfer, particularly Rayleigh–Bénard convection, is gaining importance in recent times and is the focus of the present work. Prakhar & Prosperetti (2021) formulated an Euler–Euler or two-fluid model to study the effect of highly dense point particles on the stability of Rayleigh–Bénard convection in a horizontally unbounded cell. They reported that the addition of particles into the flow increases the underlying dimensionless parameter space and stabilises the flow significantly. Recently, Raza, Hirata & Calzavarini (2024) extended this stability analysis to the suspension of bubbles in Rayleigh–Bénard convection modelled as particles by including additional forces such as added mass in the particle momentum balance equations.

In the linear analysis, we initially neglect nonlinear perturbation terms that are very small in magnitude. However, as soon as time $t = \mathcal{O}(1/c_i)$, they become $\mathcal{O}(1)$ in magnitude and cannot be neglected. Here, c_i is the growth rate. In other words, as the Rayleigh number is $Ra = g\beta\,\Delta T H^3/(\nu_f \alpha_f) > Ra_c$, the initial infinitesimally small perturbations grow exponentially and reach a magnitude that can affect the mean flow, which makes the linear stability predictions unreliable. Here, g is the gravitational acceleration, β is the thermal expansion coefficient, H is the gap between the plates, ΔT is the difference in the temperature of the bottom hot plate and the top cold plate, ν_f is the kinematic viscosity of the fluid, and α_f is the thermal diffusivity of the fluid. The nonlinear terms quench the exponential linear growth and lead to a steady or oscillating solution for Ra slightly above Ra_c (Cross & Hohenberg 1993; Cross & Greenside 2009). More generally, as Hof *et al.* (2006) mentioned, with an increase in the flow velocity, the transition from the smooth laminar to the highly disordered turbulent flow can occur through a series of instabilities during which the system can progressively lead to complicated states (Niemela *et al.* 2000), or it may occur abruptly (Grossmann 2000; Hof *et al.* 2004). Out of these two routes, Busse (2003) described a sequence of bifurcations to complex fluid flow that occurs from the simple laminar flow. Beyond the onset of convection, linear stability, in general, cannot predict the nature of instabilities and secondary flow patterns that occur in the flow field. The temporal evolution of the perturbation amplitude can be studied using nonlinear analysis. There are three approaches available for nonlinear analysis: (i) weakly nonlinear stability analysis, (ii) direct numerical simulations (DNS), and (iii) the deflation technique. Near the onset of convection, weakly nonlinear stability analysis gives valuable insights into the nature of instabilities and the secondary flow patterns with minimum computational cost compared to DNS. The deflation technique is a recent method devised to obtain the non-trivial distinct solutions of nonlinear partial differential equations (Farrell, Birkisson & Funke 2015, 2016). Using this technique, Boullé *et al.* (2022) performed the bifurcation analysis of steady states of two-dimensional Rayleigh–Bénard convection with no-slip boundary conditions.

In the current work, we use the Euler–Euler formulation given by Prakhar & Prosperetti (2021), and perform a weakly nonlinear stability analysis to study the effect of particles

on the underlying flow beyond the onset of convection near the critical point. As the perturbation amplitude grows, the nonlinear terms become significant and might lead to the phenomenon of preferential concentration of particles, which is completely absent in the linear stability analysis. Hence we study the effect of nonlinear terms on the secondary flow patterns beyond the onset of convection.

The rest of the paper is organised as follows. The problem statement and the mathematical model are given in § 2. In § 3, the linear stability analysis is provided, together with the governing equations of the basic flow and linear disturbances, and a brief review of the linear stability findings. The full formulation of the amplitude equation using weakly nonlinear stability analysis and the analysis of mutual energy exchange between fluid and particles is provided in § 4. (The numerical procedure for the present work is shown in § A.5.) The results and discussion are presented in § 5. Finally, a brief summary of the current study is given in § 6.

2. Problem statement and mathematical model

The physical model and domain with schematic representation, as shown in figure 1, consists of a continuous fluid domain $\Omega = \{(x^*, z^*) \in \mathbb{R} \times (-H/2, H/2)\}$, along with a dispersed particulate phase. Here, the bottom and the top surfaces are treated as isothermal walls maintained at temperatures T_h and T_c, respectively. The present study considers the monodispersion of very tiny spherical particles at relatively small volume fractions ($\leqslant 10^{-3}$). There are two alternative methods, called Euler–Euler and Euler–Lagrange formulations, available for the particles in the millimetre range for which the homogeneous equilibrium model fails. However, the choice of a particular method depends on various length scales, such as particle size d_p, the smallest flow length scale Δ, inter-particle separation λ, and particle number density n. When $d_p \ll \Delta \sim \lambda$ and $n\Delta^3 \gg 1$, the Euler–Lagrange formulation is preferred, whereas if $d_p \ll \lambda \ll \Delta$ and $n\Delta^3 \gg 1$, then the Euler–Euler, also called the two-fluid formulation, is preferred. The inter-particle separation λ is related to the non-dimensional particle size $\delta = (d_p/H)$ and volume fraction as $(\lambda/H) \sim (\delta/\Phi_0^{1/3})$, and, the condition becomes $\delta \ll (\delta/\Phi_0^{1/3}) \ll (\Delta/H)$. Here, in the present work, we consider the particle volume fraction $\sim 10^{-3}$, thus the first inequality, $\delta \ll (\delta/\Phi_0^{1/3})$, is satisfied. However, the second inequality is satisfied only when the particle size is $\delta \ll (\Delta/H)/\Phi_0^{1/3}$. Therefore, when $(\Delta/H) \sim 10^{-1}$ and $\Phi_0 \sim 10^{-3}$, the particle size is $\delta \ll 1$. Hence in the present work, we choose $\delta = 0.01, 0.05$. We adopt the two-fluid model given by Prakhar & Prosperetti (2021), in which the particles are introduced steadily and uniformly at the top surface at their terminal velocity with a fixed temperature. The momentum equation for the particulate phase is given by the volume-averaged Maxey–Riley–Gatignol equation (Gatignol 1983; Maxey & Riley 1983), and the thermal energy equation ensures the balance between the rate of change of the sensible heat of the particles and the rate of convective heat transfer between particulate and fluid. The dimensional independent variables (x^*, z^*, t^*) and dependent variables $(u_x^*, u_z^*, p^*, T^*, v_x^*, v_z^*, T_p^*)$ are non-dimensionalised as follows:

$$\left.\begin{aligned} &(x, z, t) = (x^*/H, z^*/H, t^*U/H), \\ &(u_x, u_z, p, \theta) = \left(u_x^*/U, u_z^*/U, p^*/\left(\rho_f U^2\right), (T - T_c)/\Delta T\right), \\ &(v_x, v_z, \theta_p) = \left(v_x^*/U, v_z^*/U, (T_p - T_c)/\Delta T\right), \end{aligned}\right\} \tag{2.1}$$

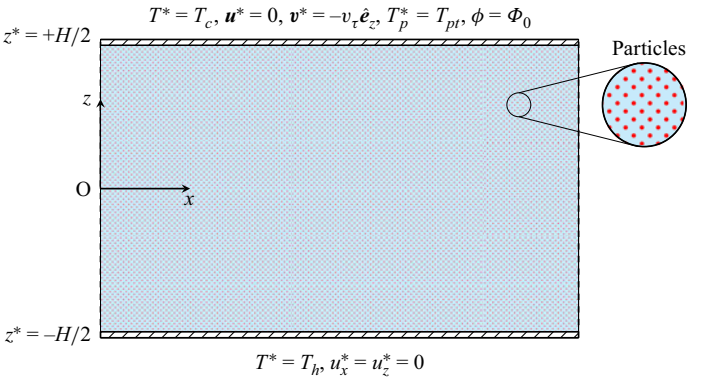

Figure 1. Schematic of the particle-laden Rayleigh–Bénard convection.

where x, z and t are the non-dimensional horizontal coordinate, vertical coordinate and time, respectively. Furthermore, u_x, u_z, p and θ are the fluid horizontal velocity component, vertical velocity component, pressure and temperature, respectively. Similarly, v_x, v_z and θ_p are dimensionless particulate phase horizontal velocity component, vertical velocity component and temperature, respectively. Here, we use the distance between the two horizontal surfaces H as a length scale, fluid free-fall velocity $U = \sqrt{g\beta\,\Delta TH}$ as a velocity scale, and the temperature difference $\Delta T = T_h - T_c$ as a temperature scale, where ρ_f, g and β are fluid density, the acceleration due to gravity and the volume expansion coefficient of fluid, respectively. The resulting governing equations in non-dimensional form are given as

$$\frac{\partial u_x}{\partial x} + \frac{\partial u_z}{\partial z} = 0, \tag{2.2}$$

$$\frac{\partial u_x}{\partial t} + u_x\frac{\partial u_x}{\partial x} + u_z\frac{\partial u_x}{\partial z} = -\frac{\partial p}{\partial x} + \sqrt{\frac{Pr}{Ra}}\nabla^2 u_x - \frac{R\phi}{St_m}(u_x - v_x), \tag{2.3}$$

$$\frac{\partial u_z}{\partial t} + u_x\frac{\partial u_z}{\partial x} + u_z\frac{\partial u_z}{\partial z} = -\frac{\partial p}{\partial z} + \sqrt{\frac{Pr}{Ra}}\nabla^2 u_z + \theta - \frac{R\phi}{St_m}(u_z - v_z), \tag{2.4}$$

$$\frac{\partial \theta}{\partial t} + u_x\frac{\partial \theta}{\partial x} + u_z\frac{\partial \theta}{\partial z} = \frac{1}{\sqrt{RaPr}}\nabla^2\theta - \frac{E\phi}{St_{th}}(\theta - \theta_p), \tag{2.5}$$

$$\frac{\partial \phi}{\partial t} + \frac{\partial(\phi v_x)}{\partial x} + \frac{\partial\,(\phi v_z)}{\partial z} = 0, \tag{2.6}$$

$$\frac{\partial v_x}{\partial t} + v_x\frac{\partial v_x}{\partial x} + v_z\frac{\partial v_x}{\partial z} = \frac{u_x - v_x}{St_m}, \tag{2.7}$$

$$\frac{\partial v_z}{\partial t} + v_x\frac{\partial v_z}{\partial x} + v_z\frac{\partial v_z}{\partial z} = \frac{u_z - v_z}{St_m} - \frac{v_0}{St_m}, \tag{2.8}$$

$$\frac{\partial \theta_p}{\partial t} + v_x\frac{\partial \theta_p}{\partial x} + v_z\frac{\partial \theta_p}{\partial z} = \frac{\theta - \theta_p}{St_{th}} \tag{2.9}$$

for all $(x, z, t) \in \{\mathbb{R} \times (-1/2, 1/2) \times (0, \infty)\}$. The boundary conditions are

$$\left.\begin{array}{l} \text{at } z = 1/2, \quad u_x = u_z = \theta = v_x = 0,\ v_z = -v_0,\ \theta_p = \Theta_{pt} \text{ and } \phi = \Phi_0, \\ \text{at } z = -1/2, \quad u_x = u_z = 0 \text{ and } \theta = 1, \end{array}\right\} \tag{2.10}$$

for all $(x, t) \in \{\mathbb{R} \times (0, \infty)\}$, where ϕ is the particle volume fraction field, and the non-dimensional parameters present in the problem, Rayleigh number Ra, Prandtl number Pr, density ratio R, specific heat capacity ratio E, mechanical Stokes number St_m, thermal Stokes number St_{th}, initial particle temperature Θ_{pt}, and non-dimensional particle terminal speed v_0, are defined as

$$\left.\begin{aligned} &Ra = g\beta\,\Delta T H^3/(\alpha_f \nu_f), \quad Pr = \nu_f/\alpha_f, \quad R = \rho_p/\rho_f, \\ &St_m = \frac{\tau_p}{\tau_f} = \frac{R\delta^2}{18 C_d}\sqrt{\frac{Ra}{Pr}}, \quad St_{th} = \frac{\tau_{th}}{\tau_f} = \frac{E\delta^2}{6Nu_p}\sqrt{RaPr}, \\ &E = R(C_{pp}/C_{pf}), \quad v_0 = \frac{Re_p}{\delta}\sqrt{\frac{Pr}{Ra}}, \quad \Theta_{pt} = \frac{T_{pt} - T_c}{T_h - T_c}, \end{aligned}\right\} \tag{2.11a–h}$$

where $\alpha_f = \kappa_f/\rho_f C_{pf}$ is the fluid thermal diffusion coefficient, $\nu_f = \mu_f/\rho_f$ is the fluid kinematic viscosity, κ_f is the fluid thermal conductivity, C_{pf} is the fluid specific heat constant, μ_f is fluid dynamic viscosity, ρ_p is the particle density, and C_{pp} is the particle specific heat. Particle diameter d_p in the non-dimensional form is represented as $\delta = d_p/H$. Introduction of particles into the flow leads to three distinct time scales: $\tau_f = H/U$ is the flow time scale, $\tau_p = \rho_p d_p^2/(18\mu_f C_d(Re_p))$ is the particle mechanical relaxation time scale, and $\tau_{th} = \rho_p C_{pp} d_p^2/(6\kappa_f\, Nu_p(Re_p, Pr))$ is the particle thermal relaxation time scale. Here, $C_d = 1 + 0.15\, Re_p^{0.687}$ is the Schiller–Naumann correction factor to the Stokes drag when the particle Reynolds number $Re_p = \rho_f v_\tau d_p/\mu_f$ is greater than unity and less than 800 (Clift, Grace & Weber 2005), $v_\tau = (1 - \rho_f/\rho_p)\tau_p g$ is the settling speed of a particle in the quiescent fluid, and $Nu_p = 2.0 + 0.6\, Re_p^{1/2}\, Pr^{1/3}$ is the particle Nusselt number. The last terms on the right-hand sides of (2.3) and (2.4) represent the mechanical two-way coupling between the fluid and particles, whereas the thermal two-way coupling is captured by the right-hand-side last term of (2.5).

3. Linear stability analysis

We assume that the fluid–particle system is at a steady state, with particles settling uniformly with their terminal velocity in a quiescent fluid. Under these conditions, the above governing equations (2.2)–(2.9) reduced to a system of ordinary differential equations, which are represented in operator form as

$$\mathcal{L}_z(P_0, \Theta_0, v_0, \Phi_0, R, St_m) = \frac{\mathrm{d}P_0}{\mathrm{d}z} - \Theta_0 + \frac{R\Phi_0}{St_m} v_0 = 0, \tag{3.1}$$

$$\mathcal{L}_\theta\big(\Theta_0, \Theta_{p0}, \Phi_0, Ra, Pr, E\big) = \frac{1}{\sqrt{RaPr}}\frac{\mathrm{d}^2\Theta_0}{\mathrm{d}z^2} - \frac{E\Phi_0}{St_{th}}\big(\Theta_0 - \Theta_{p0}\big) = 0, \tag{3.2}$$

$$\mathcal{L}_{p\theta}\big(\Theta_0, \Theta_{p0}, v_0, St_{th}\big) = \frac{\Theta_0 - \Theta_{p0}}{St_{th}} + v_0\frac{\mathrm{d}\Theta_{p0}}{\mathrm{d}z} = 0 \tag{3.3}$$

for $z \in (-1/2, 1/2)$ with boundary conditions

$$\left.\begin{aligned} &\text{at } z = 1/2, \quad \Theta_0 = 0 \text{ and } \Theta_{p0} = \Theta_{pt}, \\ &\text{at } z = -1/2, \quad \Theta_0 = 1, \end{aligned}\right\} \tag{3.4}$$

where P_0, Θ_0 and Θ_{p0} are the basic state fluid pressure, basic state fluid temperature and basic state particle temperature field, respectively, and Φ_0 is the initial uniform particle volume fraction. Using the above boundary conditions, the solution to (3.1)–(3.3) yields

the base state given by

$$\Theta_0 = \Theta_{pt} + \mathscr{A}\left[1 - (1 - lm_1)\, e^{-m_1(1/2-z)}\right] + \mathscr{B}\left[1 - (1 - lm_2)e^{-m_2(1/2-z)}\right], \tag{3.5}$$

$$\Theta_{p0} = \Theta_{pt} + \mathscr{A}\left[1 - \mathrm{e}^{-m_1(1/2-z)}\right] + \mathscr{B}\left[1 - \mathrm{e}^{-m_2(1/2-z)}\right], \tag{3.6}$$

$$\frac{\mathrm{d}P_0}{\mathrm{d}z} = \Theta_{pt} + \mathscr{A}\left[1 - (1 - lm_1)\, e^{-m_1(1/2-z)}\right] + \mathscr{B}\left[1 - (1 - lm_2)e^{-m_2(1/2-z)}\right] - \frac{R\Phi_0}{St_m} v_0, \tag{3.7}$$

where $\mathscr{A}$ and $\mathscr{B}$ are integration constants given by

$$\mathscr{A} = -\frac{(1 - \Theta_{pt})lm_2 + \Theta_{pt}\left[1 - (1 - lm_2)\, e^{-m_2}\right]}{lm_1\left[1 - (1 - lm_2)\, e^{-m_2}\right] - lm_2\left[1 - (1 - lm_1)\, e^{-m_1}\right]}, \tag{3.8}$$

$$\mathscr{B} = +\frac{(1 - \Theta_{pt})lm_1 + \Theta_{pt}\left[1 - (1 - lm_1)\, e^{-m_1}\right]}{lm_1\left[1 - (1 - lm_2)\, e^{-m_2}\right] - lm_2\left[1 - (1 - lm_1)\, e^{-m_1}\right]}. \tag{3.9}$$

Here, m_1 and m_2 are given by

$$m_1 = \frac{1}{2l}\left[1 + \sqrt{1 + 4\left(\frac{l}{L}\right)^2}\right], \quad m_2 = \frac{1}{2l}\left[1 - \sqrt{1 + 4\left(\frac{l}{L}\right)^2}\right], \tag{3.10a,b}$$

where L is the spatial non-dimensional length scale over which the effect of a particle on the surrounding fluid temperature is significant (Prakhar & Prosperetti 2021), given by

$$L = \left(\frac{St_{th}}{E\Phi_0\sqrt{RaPr}}\right)^{1/2} = \frac{\delta}{\sqrt{6\Phi_0\, Nu_p}}. \tag{3.11}$$

Here, $l = v_0 St_{th}$ is the non-dimensional length scale that the particle must traverse for its temperature to be locally equal to that of the fluid (Prakhar & Prosperetti 2021), related to other parameters as

$$l = \frac{St_{th}\, Re_p}{\delta}\sqrt{\frac{Pr}{Ra}} = \frac{E\delta\, Pr\, Re_p}{6\, Nu_p}. \tag{3.12}$$

The classical normal mode analysis (Drazin & Reid 2004) is performed to examine the stability of the basic flow mentioned above. In general, the linear stability analysis is carried out by decomposing all the dependent variables into a steady basic state and the respective infinitesimal perturbations (represented by a superscript prime):

$$\begin{aligned}\left(u_x, u_z, \theta, v_x, v_z, \theta_p, p, \phi\right) = {} & \left(0, 0, \Theta_0(z), 0, -v_0, \Theta_{p0}(z), P_0(z), \Phi_0\right) \\ & + \left(u_x', u_z', \theta', v_x', v_z', \theta_p', p', \phi'\right).\end{aligned} \tag{3.13}$$

After neglecting the higher-order terms and retaining only the first-order terms in $\{u_x', u_z', \theta', v_x', v_z', \theta_p', p', \phi'\}$, we obtain

$$\frac{\partial u_x'}{\partial x} + \frac{\partial u_z'}{\partial z} = 0, \tag{3.14}$$

$$\frac{\partial u_x'}{\partial t} = -\frac{\partial p'}{\partial x} + \sqrt{\frac{Pr}{Ra}}\nabla^2 u_x' - \frac{R\Phi_0}{St_m}\left(u_x' - v_x'\right), \tag{3.15}$$

$$\frac{\partial u_z'}{\partial t} = -\frac{\partial p'}{\partial z} + \sqrt{\frac{Pr}{Ra}}\nabla^2 u_z' + \theta' - \frac{R\Phi_0}{St_m}\left(u_z' - v_z'\right) - \frac{Rv_0}{St_m}\phi', \tag{3.16}$$

$$\frac{\partial \theta'}{\partial t} = \frac{1}{\sqrt{RaPr}}\nabla^2\theta' - u_z'\frac{\mathrm{d}\Theta_0}{\mathrm{d}z} - \frac{E\Phi_0}{St_{th}}\left(\theta' - \theta_p'\right) - \frac{E\left(\Theta_0 - \Theta_{p0}\right)}{St_{th}}\phi', \tag{3.17}$$

$$\frac{\partial \phi'}{\partial t} = v_0\frac{\partial \phi'}{\partial z} - \Phi_0\left(\frac{\partial v_x'}{\partial x} + \frac{\partial v_z'}{\partial z}\right), \tag{3.18}$$

$$\frac{\partial v_x'}{\partial t} = v_0\frac{\partial v_x'}{\partial z} + \frac{u_x' - v_x'}{St_m}, \tag{3.19}$$

$$\frac{\partial v_z'}{\partial t} = v_0\frac{\partial v_z'}{\partial z} + \frac{u_z' - v_z'}{St_m}, \tag{3.20}$$

$$\frac{\partial \theta_p'}{\partial t} = v_0\frac{\partial \theta_p'}{\partial z} + \frac{\theta' - \theta_p'}{St_{th}}. \tag{3.21}$$

The above system of equations is linear homogeneous and has the coefficient functions of spatial variables only, not dependent on time. Hence they satisfy the solution in the normal mode form given by

$$\begin{aligned}&\left(u_x', u_z', \theta', v_x', v_z', \theta_p', p', \phi'\right)^{\mathrm{T}}\\ &\quad = e^{\mathrm{i}k(x-ct)}\left(\hat{u}_x(z), \hat{u}_z(z), \hat{\theta}(z), \hat{v}_x(z), \hat{v}_z(z), \hat{\theta}_p(z), \hat{p}(z), \hat{\phi}(z)\right)^{\mathrm{T}},\end{aligned} \tag{3.22}$$

where k is the wavenumber, and $c = c_r + \mathrm{i}c_r$ is the complex wave speed corresponding to k. The sign of c_i determines the growth or decay of the disturbance. That is, as $c_i < 0$ or $c_i = 0$ or $c_i > 0$, the flow is stable or neutrally stable or unstable, respectively. Substitution of (3.22) in (3.14)–(3.21) leads to linearised disturbance equations in operator form given in the § A.1. The boundary conditions for corresponding equations are given by

$$\left.\begin{aligned}&\text{at } z = 1/2, \quad \hat{u}_x = \hat{u}_z = \hat{\theta} = \hat{v}_x = \hat{v}_z = \hat{\theta}_p = \hat{\phi} = 0,\\ &\text{at } z = -1/2, \quad \hat{u}_x = \hat{u}_z = \hat{\theta} = 0.\end{aligned}\right\} \tag{3.23}$$

The system of linear equations (A1)–(A8) together with the boundary conditions gives rise to a generalised eigenvalue problem given by

$$\mathbb{A}\boldsymbol{q} = c\mathbb{B}\boldsymbol{q}, \tag{3.24}$$

where $\boldsymbol{q} = (\hat{u}_x, \hat{u}_z, \hat{\theta}, \hat{v}_x, \hat{v}_z, \hat{\theta}_p, \hat{p}, \hat{\phi})$ is the eigenfunction corresponding to the eigenvalue c, and $\mathbb{A}, \mathbb{B}$ are the square complex matrices. The fundamental disturbance is given by $\boldsymbol{q}\, e^{\mathrm{i}k(x-c_r t)}$, where $\boldsymbol{q}$ is the eigenfunction related to the least stable eigenvalue, and c_r is the corresponding wave speed. (Several parts of the weakly nonlinear analysis will employ the frequent use of the fundamental disturbance.)

The bifurcation point, also known as the critical point (k, Ra), and the shape of the emerging disturbances are both determined using the linear stability theory. It offers no information regarding the actual magnitude of the disturbances (amplitude) away from the critical value. A weakly nonlinear stability study is necessary to examine the amplitude of

such disturbances. The outcomes of the linear stability analysis are also necessary for a nonlinear analysis.

There have been two studies (Prakhar & Prosperetti 2021; Raza *et al.* 2024) on the linear stability analysis of the present problem in the literature. Using a two-fluid model, Prakhar & Prosperetti (2021) studied the stability threshold of particle-laden Rayleigh–Bénard convection when the particles are much denser than the underlying fluid. Raza *et al.* (2024) extended the two-fluid model by Prakhar & Prosperetti (2021) to lighter particles such as bubbles by adding an added-mass term. Using dimensional analysis, we can show that eight independent dimensionless parameters exist in this problem, such as Rayleigh number Ra, Prandtl number Pr, density ratio R, heat capacity ratio E, particle Reynolds number Re_p, particle diameter δ, particle injection temperature Θ_{pt}, and initial particle volume fraction Φ_0. We fix the dimensionless parameters such as Prandtl number $Pr = 0.71$, density ratio $R = 800$, and specific heat capacity ratio $E = 3385$, such that the fluid–particle system represents the water droplets suspended in dry air.

We present the linear stability results for the air–water droplet system. The effect of initial particle volume fraction on the critical Rayleigh number Ra_c and the critical wavenumber k_c for different particle Reynolds numbers Re_p and the particle sizes δ is shown in figure 2(*a*,*b*). The critical Rayleigh number increases with Φ_0 for all Re_p and δ. This stabilisation of the flow under the presence of particles is due to the dissipative nature of the mechanical and thermal two-way coupling source terms in (2.3)–(2.4) and (2.5), respectively. The strength of the mechanical source terms is proportional to $(R\Phi_0/St_m) \sim \Phi_0 C_d/\delta^2$, independent of the density ratio R. Similarly, the strength of the thermal source term is proportional to $E\Phi_0/St_{th} \sim \Phi_0\, Nu_p/\delta^2$, which is independent of the heat capacity ratio E. Hence with an increase in the Φ_0 value (decrease in δ value) in either source term, the dissipation increases and thereby increases the stability (increase in Ra_c value). However, the increase in Ra_c with Φ_0 is more significant for smaller particles ($\delta = 0.01$), due to the strong $1/\delta^2$ dependence of the two-way coupling source terms, than for the large particles ($\delta = 0.05$). Moreover, the weak dependency of the mechanical and thermal source terms on particle Reynolds number Re_p through drag force coefficient C_d and the Nusselt number Nu_p explains the small increase in Ra_c with the increase in Re_p. Similarly, from figure 2(*b*), it is clear that the critical wavenumber k_c increases with an increase in Φ_0 for all Re_p and δ. The plausible explanation for this can be obtained using the inter-particle distance $\lambda/H \sim (1-\Phi_0)^{1/3}\delta/\Phi_0^{1/3} \approx \delta/\Phi_0^{1/3}$ for the dilute suspensions ($\Phi_0 \ll 1$) (Prakhar & Prosperetti 2021). Hence the critical wavenumber can be expected to vary as $k_c \sim \Phi_0^{1/3}/\delta$, which explains the increase of k_c with an increase in Φ_0 for all Re_p and δ values. We note that the increase in k_c is significant for the small particles ($\delta = 0.01$) with small Reynolds number $Re_p = 1$ rather than for the large particles ($\delta = 0.05$) with large Reynolds number $Re_p = 10$ as shown in figure 2(*b*).

The effect of particle injection temperature Θ_{pt} on the critical parameters and the base-state fluid temperature is shown in figure 3(*a–d*). In figure 3(*a*), the present data are compared with the existing work by Prakhar & Prosperetti (2021). It is observed that with an increase in Θ_{pt}, the critical Rayleigh number Ra_c increases in the initial part of figure 3(*a*). The explanation for this is that the particles act as the sources of heat, and by increasing their temperature, they tend to reduce the thermal stratification inside the domain, leading to an increase in the stability of the flow. However, from figure 3(*c*), it is clear that as the particle temperature increases beyond $\Theta_{pt} > 1$, the strong negative base-state temperature gradients start to appear in the upper part of the domain, and favour the instability. The effect of Θ_{pt} on the critical wavenumber is shown in figure 3(*b*). As Θ_{pt} is increased from -1 to 2, k_c decreases until $\Theta_{pt} \approx 0.5$, then increases monotonically.

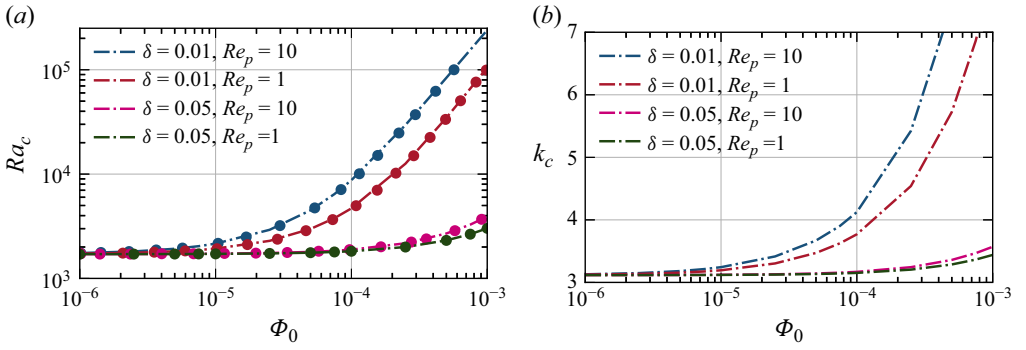

Figure 2. Effect of initial particle volume fraction on critical Rayleigh number Ra_c and critical wavenumber k_c: (*a*) variation in critical Rayleigh number Ra_c, and (*b*) variation in critical wavenumber k_c with initial undisturbed particle volume fraction Φ_0 for two different particle Reynolds numbers Re_p and particle sizes δ, and other parameters kept at $\Theta_{pt} = 0$, $R = 800$, $E = 3385$ and $Pr = 0.71$ for both graphs. Here, the circles represent data from Prakhar & Prosperetti (2021).

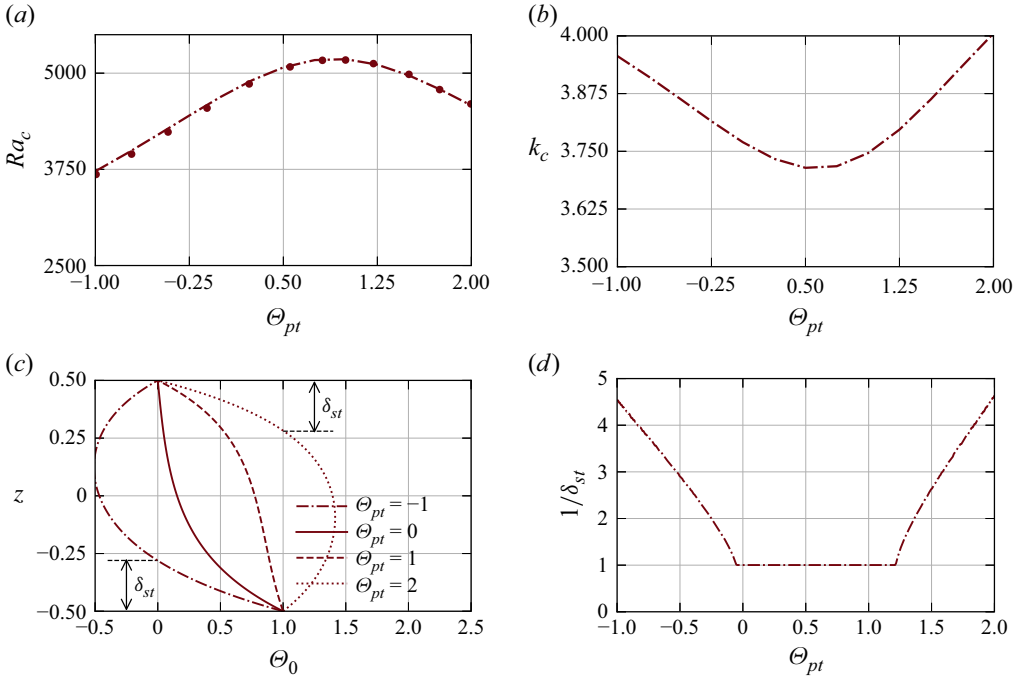

Figure 3. Effect of particle injection temperature Θ_{pt} on critical parameters, base-state fluid temperature and its stratification. (*a*) Variation in critical Rayleigh number Ra_c, where the dots represent the data from Prakhar & Prosperetti (2021). (*b*) Variation in critical wavenumber k_c. (*c*) Variation in base-state fluid temperature. (*d*) Variation in unstably stratified layer thickness δ_{st} with particle injection temperature. Here, $Re_p = 1$, $\delta = 0.01$, $\Phi_0 = 10^{-4}$, $R = 800$, $E = 3385$ and $Pr = 0.71$ for all graphs.

This can be explained by looking at the variation in unstably stratified layer thickness δ_{st} in the base-state temperature profile shown in figure 3(*c*) and 3(*d*). For $\Theta_{pt} = -1$ in figure 3(*c*), from $z \approx -0.26$ to -0.5, the fluid is unstably stratified over thickness δ_{st}, and in the remaining domain, Θ_{pt} has a symmetric distribution. A similar distribution exists for $\Theta_{pt} = 2$, but the unstably stratified layer exists near the cold top surface. The thickness

of this unstably stratified layer increases for $\Theta_{pt} = -1$ to $\Theta_{pt} \approx 0$, maintains a constant total height $\delta_{st} = 1$ from $\Theta_{pt} \approx 0$ to $\Theta_{pt} \approx 1.25$, and subsequently increases monotonically for $\Theta_{pt} \approx 1.25$ to $\Theta_{pt} = 2$. From the definition of δ_{st}, we note that the non-dimensional temperature difference across all these unstably stratified layers is 1. Hence an increase in δ_{st} value with the same temperature difference results in a lower temperature gradient, favouring stability. This explains the initial increase in Ra_c value in figure 3(*a*). From $\Theta_{pt} \approx 1.25$ to $\Theta_{pt} = 2$, the unstable stratified layer thickness reduces, maintaining the same temperature difference across its length, which increases the negative temperature gradient and favours the instability. Hence Ra_c reduces from $\Theta_{pt} \approx 1.25$ onwards. It should be noted that k_c represents the length scale for the onset of convection, and it changes with particle volume fraction Φ_0 and size δ. However, in this case, we keep Φ_0 and δ constant, and vary only Θ_{pt}. Hence the explanation for the non-monotonic variation of k_c with Θ_{pt} can be deduced from the variation of δ_{st} with Θ_{pt} shown in figure 3(*d*). As δ_{st} increases, the length scale at the onset of convection increases, leading to a decrease in k_c, and vice versa.

4. Formulation of finite amplitude equations

In the present work, the finite amplitude expansions are given based on the analysis of Stuart (1960), Yao & Rogers (1992), Khandelwal & Bera (2015), Sharma, Khandelwal & Bera (2018) and Aleria, Khan & Bera (2024). The Fourier expansion of fluid temperature θ in separable form is

$$\begin{aligned}\theta(x, z, t) &= \Theta(z, \tau)\,\mathbb{E}^0 + \hat{\theta}_1(z, \tau)\,\mathbb{E}^1 + \hat{\theta}_2(z, \tau)\,\mathbb{E}^2 + \cdots + \text{c.c.} \\ &= \mathbb{E}^0\left[\Theta_0(z) + c_i\,|B(\tau)|^2\,\Theta_1(z) + \mathcal{O}\left(c_i^2\right)\right] \\ &\quad + \mathbb{E}^1\left[c_i^{1/2}\,B(\tau)\,\theta_{10}(z) + c_i^{3/2}\,B(\tau)\,|B(\tau)|^2\,\theta_{11}(z) + \mathcal{O}\left(c_i^{5/2}\right)\right] \\ &\quad + \mathbb{E}^2\left[c_i\,B(\tau)^2\,\theta_{20}(z) + \mathcal{O}\left(c_i^2\right)\right] + \cdots + \text{c.c.},\end{aligned} \tag{4.1}$$

where $\mathbb{E}^j = \exp(j[\mathrm{i}k_c(x - c_r t)])$ for $j = 0, 1, 2$, k_c is the wavenumber corresponding to the critical Rayleigh number Ra_c, and c_r is the real part of c corresponding to the most unstable disturbance. The amplitude function B will be obtained from the Landau equation, and c.c. stands for the complex conjugate of the complex-valued functions (the second and third terms).

The evolution equation for the slowly varying amplitude B is derived using the method of multiple time scales. Hence two distinct time scales (a fast time scale t and a slow time scale τ) are used in the nonlinear stability analysis of the flow. As in linear stability analysis, the exponential variation of disturbance amplitude is associated with the fast time scale. As the disturbance amplitude grows exponentially and attains a finite amplitude, the nonlinear terms become important. This leads to the deviation of the temporal exponential growth of the disturbances. Hence another time scale (the slow time scale) is needed to capture the effect of nonlinearities of different orders. The slow time scale is defined as $\tau = c_i t$, with c_i being the growth rate of the most unstable disturbance obtained from the linear stability analysis. Hence the derivative with respect to t of a function $f(t) = F(t, \tau)$ is given by

$$\frac{\partial f}{\partial t} = \frac{\partial F}{\partial t} + c_i \frac{\partial F}{\partial \tau}. \tag{4.2}$$

Thus for a function of the form $F(t, \tau)$, both t and τ are treated as if they are independent variables. The justification of (4.1) is as follows. From the linear theory, it is known that the growth rate c_i is linearly proportional to $(Ra - Ra_c)/Ra_c$, the Rayleigh number

difference from the neutral curve. Using a finite amplitude stability analysis for the Rayleigh–Bénard convection (Schlüter *et al.* 1965) and for the non-isothermal flow in a vertical annulus, Yao & Rogers (1992) showed that the square of equilibrium amplitude A_e^2 is proportional to $(Ra - Ra_c)/Ra_c$, and consequently the equilibrium amplitude is proportional to $c_i^{1/2}$, with a proportionality constant that is a weak function of Ra near Ra_c. Hence the amplitude of the disturbance fluid temperature θ_{10} with wavenumber k_c is of the order of $c_i^{1/2}$. The amplitude of the disturbances of higher harmonics is chosen based on the number of interactions between lower-order harmonics. For example, the harmonic with wavenumber $2k_c$ needs two disturbances with wavenumber k_c, which gives its amplitude of order c_i. Similarly, the higher-order correction to the base state results from the Reynolds stress due to the interaction of $\mathbb{E}^1$ and its complex conjugate $\mathbb{E}^{-1}$ with an amplitude of order c_i (Stewartson & Stuart 1971).

4.1. *Derivation of the cubic Landau equation*

Substitute the perturbation series similar to (4.1) for all the dependent variables in (2.2)–(2.9), and separate the harmonic components. The resulting equations are shown in § A.2. The first Landau coefficient does not depend on the higher-order harmonics ($\mathbb{E}^3$, $\mathbb{E}^4$ etc.). Therefore, those terms are ignored in the series (4.1). The systems of equations at different harmonics (A9)–(A13), (A15)–(A22) and (A23)–(A30) are solved at increase orders of c_i. At $\mathcal{O}(c_i^0)$, $\mathbb{E}^0$ harmonic equations are identical to the basic-flow equations (3.1)–(3.3). At $\mathcal{O}(c_i)^{1/2}$, $\mathbb{E}^1$ equations are similar to that of linear stability (A1)–(A8), and the $\mathbb{E}^0$ and $\mathbb{E}^2$ do not contribute at this order. The functions u_{x10}, u_{z10}, θ_{10}, v_{x10}, v_{z10}, θ_{p10} and ϕ_{10} are the eigenfunctions of linear stability equations at a particular wavenumber and Rayleigh number Ra. At $\mathcal{O}(c_i)$, $\mathbb{E}^0$ and $\mathbb{E}^2$ generate the system of non-homogeneous equations for basic-flow distortion functions Θ_1, Θ_{p1}, V_1 and Φ_1, and the functions u_{x20}, u_{z20}, θ_{20}, v_{x20}, v_{z20}, θ_{p20} and ϕ_{20}, respectively. These equations contain the non-homogeneous part made up of known functions u_{x10}, u_{z10}, θ_{10}, v_{x10}, v_{z10}, θ_{p10}, ϕ_{10} and their derivatives, which are obtained at lower-order computations. At $\mathcal{O}(c_i^{3/2})$, the $\mathbb{E}^1$ harmonic results in a non-homogeneous system of equations with linear stability operators acting on the functions u_{x11}, u_{z11}, θ_{11}, v_{x11}, v_{z11}, θ_{p11} and ϕ_{11}. However, the right-hand-side non-homogeneous part contains the terms proportional to the unknown terms $\mathrm{d}B/\mathrm{d}\tau$, B and $B\,|B|^2$, with coefficients depending on functions known from the lower-order analysis. The Fredholm alternative solvability condition is imposed on the non-homogeneous right-hand side of the $\mathbb{E}^1$ harmonic at $\mathcal{O}(c_i^{3/2})$ to obtain a non-trivial solution. To impose the solvability condition, the solution to the homogeneous adjoint system (see § A.4) corresponding to the linear stability operator is required. Accordingly, the non-homogeneous right-hand side must be orthogonal to the adjoint functions $\hat{u}_x^\dagger$, $\hat{u}_z^\dagger$, $\hat{\theta}^\dagger$, $\hat{v}_x^\dagger$, $\hat{v}_z^\dagger$, $\hat{\theta}_p^\dagger$ and $\hat{\phi}^\dagger$. The orthogonality is imposed by multiplying the right-hand side of the system of linear equations of $\mathbb{E}^1$ harmonic functions at $\mathcal{O}(c_i^{3/2})$ with $(\hat{p}^\dagger, \hat{u}_x^\dagger, \hat{u}_z^\dagger, \hat{\theta}^\dagger, \hat{\phi}^\dagger, \hat{v}_x^\dagger, \hat{v}_z^\dagger, \hat{\theta}_p^\dagger)$, and integrating with respect to z from $-1/2$ to $1/2$, which gives the cubic Landau equation

$$\frac{\mathrm{d}B}{\mathrm{d}\tau} = k_c B + a_1 B\,|B|^2, \tag{4.3}$$

where a_1 is the Landau constant defined as

$$a_1 = -\int_{-1/2}^{1/2} \left(\mathcal{G}_x \hat{u}_x^\dagger + \mathcal{G}_z \hat{u}_z^\dagger + \mathcal{G}_\theta \hat{\theta}^\dagger + \mathcal{G}_\phi \hat{\phi}^\dagger + \mathcal{G}_{px} \hat{v}_x^\dagger + \mathcal{G}_{pz} \hat{v}_z^\dagger + \mathcal{G}_{p\theta} \hat{\theta}_p^\dagger\right) \mathrm{d}z, \tag{4.4}$$

which represents the first correction to the growth rate given by linear stability analysis.

By changing the variables as $A = c_i^{1/2} B$ and $\tau = c_i t$ in (4.3),

$$\frac{\mathrm{d}A}{\mathrm{d}t} = k_c c_i A + a_1 A^2 \tilde{A}, \tag{4.5}$$

and its corresponding complex conjugate equation is

$$\frac{\mathrm{d}\tilde{A}}{\mathrm{d}t} = k_c c_i \tilde{A} + \tilde{a}_1 \tilde{A}^2 A, \tag{4.6}$$

where $k_c c_i$ is the growth rate from the linear stability analysis, and A is the physical amplitude of the wave. Multiply (4.5) with $\tilde{A}$ and (4.6) with A and add them:

$$\frac{\mathrm{d}|A|^2}{\mathrm{d}t} = 2k_c c_i \, |A|^2 + 2\,\mathrm{Re}\{a_1\}\,|A|^4, \tag{4.7}$$

where $\mathrm{Re}\{a_1\}$ is the real part of a_1. Equation (4.7) has an equilibrium amplitude A_e as a solution if

$$\frac{\mathrm{d}|A|}{\mathrm{d}t} = 0. \tag{4.8}$$

Consequently, three possible equilibrium amplitudes exist:

$$A_e = 0 \quad and \quad A_e = \pm\sqrt{-k_c c_i / \mathrm{Re}\,\{a_1\}}. \tag{4.9a,b}$$

Here, $A_e = 0$ represents the steady base flow, which is stable for $Ra < Ra_c$ and unstable for $Ra > Ra_c$, and Ra_c is the critical Rayleigh number obtained from linear stability analysis. From (4.9), the existence of a finite amplitude solution is guaranteed if $k_c c_i$ and $\mathrm{Re}\{a_1\}$ have opposite signs (Drazin & Reid 2004; Shukla & Alam 2011). Therefore, there are two possibilities: first, the growth rate is positive (for $Ra > Ra_c$), and the real part of the Landau constant is negative; second, the growth rate is negative (for $Ra < Ra_c$), and the real part of the Landau constant is positive. The first possibility leads to a supercritical pitchfork bifurcation, whereas the second possibility leads to a subcritical pitchfork bifurcation.

Using equilibrium amplitude definition (4.9*b*), (4.7) can be rewritten as

$$\frac{\mathrm{d}|A|^2}{\mathrm{d}t} = 2\,\mathrm{Re}\,\{a_1\}\,|A|^2\big(|A|^2 - A_e^2\big), \tag{4.10}$$

where $A_e^2 = -(k_c c_i)/\mathrm{Re}\{a_1\}$. The solution for the above equation is

$$|A|^2 = \frac{A_e^2}{1 + \left(\dfrac{A_e^2}{|A_0|^2} - 1\right) e^{-2k_c c_i t}}, \tag{4.11}$$

where $|A_0|$ is the value of $|A|$ at $t = 0$. From (4.11), it is clear that when $Ra > Ra_c$, as $t \to \infty$, $|A| \to A_e$. Hence, irrespective of the initial amplitude $|A_0|$, the amplitude eventually tends to the equilibrium amplitude A_e. Multiply (4.5) with $1/\tilde{A}$ and (4.6) with $-A/\tilde{A}^2$, and add them:

$$\frac{\mathrm{d}}{\mathrm{d}t}\left(\frac{A}{\tilde{A}}\right) = 2\mathrm{i}A^2\,\mathrm{Im}\{a_1\}, \tag{4.12}$$

where $\mathrm{Im}\{a_1\}$ is the imaginary part of a_1. The above equation can be rewritten as

$$\frac{\mathrm{d}\left(\dfrac{A}{\tilde{A}}\right)}{\left(\dfrac{A}{\tilde{A}}\right)} = 2\mathrm{i}\,\mathrm{Im}\{a_1\}\,|A|^2\,\mathrm{d}t. \tag{4.13}$$

Hence the solution for A is given by

$$\frac{A}{A_0} = \frac{|A|}{|A_0|} \exp\left\{ \mathrm{i}\,\mathrm{Im}\{a_1\} \int_0^t |A|^2 \,\mathrm{d}t \right\}, \tag{4.14}$$

where $|A|(t)$ is given by the square root of (4.11). The closed-form solution for amplitude function $A(t)$ is obtained by integrating the above equation:

$$\frac{A(t)}{A_0} = \frac{|A|}{|A_0|} \left\{ \frac{|A|}{|A_0|}\, e^{-k_c c_i t} \right\}^{\mathrm{i}\,\mathrm{Im}\{a_1\}/\mathrm{Re}\{a_1\}}, \tag{4.15}$$

where $|A|(t)$ is obtained from (4.11).

4.2. *Heat flux balance*

The solution to the Landau equation given by (4.11) and (4.15) shows the existence of a steady-state solution as $t \to \infty$. Hence in this subsection, we derive an equation for the average heat flux balance at steady state. At steady state, integrating the fluid energy (2.5) in the domain $(x, z) \in \{(-0.5, 0.5) \times (-\pi/k_c, \pi/k_c)\}$ yields

$$\begin{aligned} &\int_{z=-0.5}^{0.5} \int_{x=-\pi/k_c}^{\pi/k_c} \left(u_x \frac{\partial \theta}{\partial x} + u_z \frac{\partial \theta}{\partial z} \right) \mathrm{d}x\, \mathrm{d}z \\ &\quad = \int_{z=-0.5}^{0.5} \int_{x=-\pi/k_c}^{\pi/k_c} \left(\frac{1}{\sqrt{RaPr}} \left(\frac{\partial^2 \theta}{\partial x^2} + \frac{\partial^2 \theta}{\partial z^2} \right) - \frac{E\phi}{St_{th}} (\theta_p - \theta_p) \right) \mathrm{d}x\, \mathrm{d}z. \end{aligned} \tag{4.16}$$

Since u_x, u_z, θ and θ_p are periodic functions in x with period $2\pi/k$, the non-zero contribution comes only from the $\mathbb{E}^0$ harmonic. Hence (4.16) is essentially equivalent to the integration of $\mathbb{E}^0$ harmonic (A10) in $z \in (-0.5, 0.5)$. Therefore, after substituting $A_e^2 = c_i\,|B|^2$, $\Theta = \Theta_0 + A_e^2 \Theta_1$ and $\Theta_p = \Theta_{p0} + A_e^2 \Theta_{p1}$ in (A10), we have

$$\begin{aligned} &\int_{z=-0.5}^{0.5} \frac{\mathrm{d}^2 \Theta}{\mathrm{d}z^2}\, \mathrm{d}z \\ &= E\sqrt{RaPr} \int_{z=-0.5}^{0.5} \left\{ \Phi_0 \frac{\Theta - \Theta_p}{St_{th}} + A_e^2 \Phi_1 \frac{\Theta_0 - \Theta_{p0}}{St_{th}} + A_e^2 \frac{\mathrm{d}}{\mathrm{d}z} \left(\tilde{\theta}_{10} u_{z10} + \theta_{10} \tilde{u}_{z10} \right) \right\} \mathrm{d}z, \end{aligned} \tag{4.17}$$

where the integral of the last term on the right-hand side goes to zero because $u_{z10} = \theta_{10} = 0$ at $z = -0.5$ and 0.5. From (A13), we have the identities

$$\frac{\Theta - \Theta_p}{St_{th}} = -v_0 \frac{\mathrm{d}\Theta_p}{\mathrm{d}z} + A_e^2 V_1 \frac{\mathrm{d}\Theta_{p0}}{\mathrm{d}z}, \tag{4.18}$$

$$\frac{\Theta_0 - \Theta_{p0}}{St_{th}} = -v_0 \frac{\mathrm{d}\Theta_{p0}}{\mathrm{d}z}. \tag{4.19}$$

Hence (4.17) simplifies to

$$[\![Nu]\!] = v_0 E \Phi_0 \sqrt{RaPr}\, [\![\Theta_p]\!] + A_e^2 \int_{z=-0.5}^{0.5} (\Phi_0 V_1 - \Phi_1 v_0) \frac{\mathrm{d}\Theta_{p0}}{\mathrm{d}z}\, \mathrm{d}z, \tag{4.20}$$

where the bracket is defined for the function $f(z)$ as $[\![f]\!] = f(0.5) - f(-0.5)$, and $Nu_h = Nu(-0.5) = -\mathrm{d}\Theta/\mathrm{d}z\big|_{z=-0.5}$ and $Nu_c = Nu(0.5) = -\mathrm{d}\Theta/\mathrm{d}z\big|_{z=0.5}$ are the Nusselt numbers (or non-dimensional heat fluxes) at the hot and cold surfaces, respectively. It can be shown that the solution to the linearised volume fraction equation is always zero

(see § A.6). Hence from (A11),

$$\frac{\mathrm{d}}{\mathrm{d}z}(\Phi_0 V_1 - \Phi_1 v_0) = 0 \tag{4.21}$$

for $z \in (-0.5, 0.5)$. Therefore, from (4.20) and (4.21), the net flux balance is given by

$$[\![Nu]\!] = v_0 E \Phi_0 \sqrt{RaPr}\,[\![\Theta_p]\!], \tag{4.22}$$

where the proportionality constant $v_0 E \Phi_0 \sqrt{RaPr}$ is equal to L^2/l. Here, L and l are the non-dimensional length scales given by (3.11) and (3.12), respectively. Thus the alternate form of the above equation is given by

$$[\![Nu]\!] = [\![Q_p'']\!], \tag{4.23}$$

where $Q_{ph}'' = Q_p''(-0.5) = (l/L^2)\,\Theta_p(-0.5)$ and $Q_{pc}'' = Q_p''(0.5) = (l/L^2)\,\Theta_p(0.5)$ are the non-dimensional particle sensible heat fluxes at hot and cold surfaces, respectively. The physical significance of (4.23) is that at steady state, the net heat flux released from the hot and cold surfaces is equal to the net sensible heat exchanged by the particles. Therefore, for the single-phase and particle-laden flows without thermal energy two-way coupling, the heat flux at the hot surface is exactly the heat flux at the cold surface. However, for the problems with thermal energy two-way coupling, the two phases exchange the heat by following (4.23), and heat fluxes Nu at hot and cold need not be equal.

5. Results and discussion

We carry out the analysis of the effect of the nonlinear interactions of different harmonics on the equilibrium amplitude, rate of heat transfer and the pattern of secondary flow. All the analysis is done near the bifurcation point such that the perturbation series (4.1) is valid. We define a new parameter called the reduced Rayleigh number, $\delta_{Ra} = (Ra - Ra_c)/Ra_c$, which quantifies the deviation from the bifurcation point Ra_c.

5.1. *Effect of particle volume fraction*

The grid independence test on the growth rate c_i, the real part of the Landau constant $\mathrm{Re}\{a_1\}$, and the equilibrium amplitude A_e for $\delta_{Ra} \in [0, 0.75]$ at three different particle volume fractions with corresponding critical wavenumbers is shown in table 1. With an increase in the degree of the Chebyshev polynomial N, the values of c_i, $\mathrm{Re}\{a_1\}$ and A_e are not changed consistently for each Φ_0 value. Hence we fix $N = 50$ for all the computations in the present work. Moreover, it can be seen that the growth rate c_i is positive and decreases with an increase in Φ_0, $\mathrm{Re}\{a_1\} < 0$, and A_e also decreases with an increase in Φ_0. These observations are more apparent in figure 4(*a–c*), in which c_i, $\mathrm{Re}\{a_1\}$, A_e and $A_e/\sqrt{c_i}$ are plotted against δ_{Ra} at four different Φ_0 values. Figure 4(*a*) shows the linear variation of c_i with δ_{Ra} near the critical point. The decrease in c_i value with an increase in Φ_0 reveals that the stability of the flow increases with an increase in particle volume fraction. The real part of the Landau constant satisfies $\mathrm{Re}\{a_1\} < 0$ for $\delta_{Ra} \in [0, 0.75]$ at all Φ_0 values (see figure 4*b*). Hence $\mathrm{Re}\{a_1\} < 0$ together with $c_i > 0$ for $\delta_{Ra} > 0$ shows the supercritical pitchfork bifurcation at the critical point. Therefore, the stable, positive and finite equilibrium amplitude A_e is guaranteed (Drazin & Reid 2004; Shukla & Alam 2011). In the present work on particle-laden Rayleigh–Bénard convection, the real part of the wave speed c_r of the most dominant disturbance, and the imaginary part of the Landau constant $\mathrm{Im}\{a_1\}$ are always zero. Hence from (4.1) and (4.15), we expect the steady-state equilibrium solutions near the critical point $\delta_{Ra} \in (0, 0.75)$ as $t \to \infty$.

Φ_0	N	c_i	$Re\{a_1\}$	A_e
10^{-5}	30	0.0095822260252546	−2.5036981432421341	0.1105637883706295
	40	0.0095822260247759	−2.5036981431506380	0.1105637883698877
	50	0.0095822260222355	−2.5036981431784873	0.1105637883546169
	60	0.0095822260252879	−2.5036981430774201	0.1105637883744580
10^{-4}	30	0.0080109706070805	−3.1611749067227288	0.0977402064516451
	40	0.0080109706065269	−3.1611749067584540	0.0977402064477159
	50	0.0080109706064721	−3.1611749068802188	0.0977402064454993
	60	0.0080109706072748	−3.1611749065909187	0.0977402064548681
10^{-3}	30	0.0044982008778323	−5.5363083852835402	0.0802866894011331
	40	0.0044982008776943	−5.5363086210155394	0.0802866876906275
	50	0.0044982008777145	−5.5363086208461425	0.0802866876920357
	60	0.0044982008776811	−5.5363086210110506	0.0802866876905422

Table 1. Grid independence test on growth rate c_i, real part of Landau constant $\mathrm{Re}\{a_1\}$ and equilibrium amplitude A_e for $Re_p = 1$, $\delta = 0.01$, $R = 800$, $E = 3385$, $Pr = 0.71$, $\Theta_{pt} = 0$ and $\Phi_0 = \{10^{-5}, 10^{-4}, 10^{-3}\}$ at $\delta_{Ra} = 0.1$.

Here, $c_r = \mathrm{Im}\{a_1\} = 0$ can be argued physically from the symmetries of the present problem. The real part of the complex wave speed c_r represents the speed and the direction of propagation of the disturbance in the flow. However, there is no preferential direction for the flow due to the absence of a non-zero base state fluid velocity. In other words, the clockwise and anticlockwise steady rolls are the solutions to the problem, which is possible only if $c_r = 0$ for the most unstable disturbance. Moreover, the present problem is invariant under translation along the horizontal direction due to its infinite extent $x \in (-\infty, \infty)$, and $\mathrm{Im}\{a_1\}$ represents the phase angle of amplitude (see (4.14)), which captures a finite spatial shift along the horizontal direction that leads to $\mathrm{Im}\{a_1\} = 0$.

The supercritical bifurcation at the critical point leads to an equilibrium amplitude A_e, which varies with control parameter δ_{Ra} without any hysteresis as shown in figure 4(*c*). Since $c_i \propto \delta_{Ra}$, and from (4.9*b*) it is clear that $A_e \propto \sqrt{c_i}$, A_e shows a square root dependency on δ_{Ra} near the critical point, as shown in figure 4(*c*). Moreover, with increase in Φ_0, for a given δ_{Ra}, the growth rate c_i decreases with a nearly constant $\mathrm{Re}\{a_1\}$ for $\Phi_0 = 10^{-6}$, 10^{-5}, and 10^{-4}. However, for $\Phi_0 = 10^{-3}$, a significant decrease in $\mathrm{Re}\{a_1\}$ is observed. Therefore, from (4.9*b*) for the equilibrium amplitude, A_e decreases with an increase in Φ_0. In the present study, $A_e \sim \sqrt{c_i}$ is the primary assumption in writing perturbation series (4.1) for all the dependent variables, which is shown in figure 4(*d*). The nature of nonlinearity with supercritical bifurcation is to quench or saturate the exponential growth predicted by the linear analysis (Hoyle 2006; Cross & Greenside 2009), and leads to a finite amplitude equilibrium solution. In the present work, the magnitude of nonlinear effects is proportional to $\mathrm{Re}\{a_1\}$ in the cubic Landau equation (4.7). The growth rate c_i decreases with an increase in particle volume fraction, as shown in figure 4(*a*), beyond the critical point. Hence the stability of the system is increasing with an increase in Φ_0. The same physical phenomenon of increasing stabilisation is reflected in the weakly nonlinear regime through an increase in the magnitude of $\mathrm{Re}\{a_1\}$, as shown in figure 4(*b*). Here, the more negative $\mathrm{Re}\{a_1\}$, the more rapid quenching/saturation of exponential growth beyond the critical point.

The effect of particle volume fraction Φ_0 on the heat transfer measured as the mean value of $[\![Nu]\!]$ for $\delta_{Ra} \in (0.0, 0.1)$ is shown in table 2. The Nusselt numbers at the hot Nu_h and cold Nu_c surfaces are unequal due to the thermal energy coupling between the particles and fluid. As shown in (4.23), the difference between Nu_h and Nu_c is balanced by the

Φ_0	$\overline{[\![Nu]\!]}$
10^{-6}	0.0615
10^{-5}	0.5679
10^{-4}	3.4641
10^{-3}	13.9429

Table 2. Effect of particle volume fraction on heat transfer near the bifurcation point. Here, $\overline{[\![Nu]\!]}$ represents the average value of $[\![Nu]\!]$ at a given particle volume fraction Φ_0 and $\delta_{Ra} \in (0, 0.1)$. Other parameters are kept constant at $\delta = 0.01$, $Re_p = 1$, $R = 800$, $E = 3385$, $\Theta_{pt} = 0$ and $Pr = 0.71$.

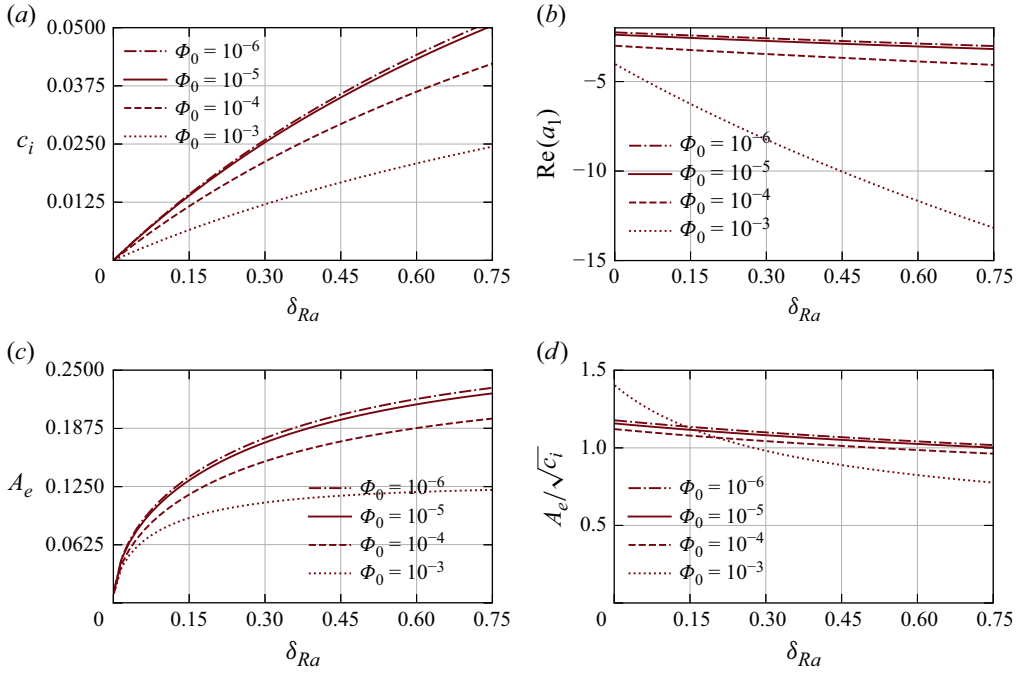

Figure 4. Effect of particle volume fraction near the bifurcation point: (*a*) variation of growth rate, (*b*) real part of Landau constant, (*c*) equilibrium amplitude, and (*d*) ratio of equilibrium amplitude and the square root of growth rate with reduced Rayleigh number δ_{Ra}, for other parameters kept at $\delta = 0.01$, $Re_p = 1$, $R = 800$, $E = 3385$ and $Pr = 0.71$.

convective sensible heat flux by the particles at hot (Q''_{ph}) and cold (Q''_{pc}) surfaces. Here, the particles are introduced into the domain at the cold surface temperature ($\Theta_{pt} = 0$). Hence sensible heat flux by particles at the cold surface is $Q''_{pc} = 0$. As the particle concentration increases, the difference between the heat fluxes at the hot and cold surfaces for fluid and particles increases. Thus the Nusselt number at the hot surface increases, while at the cold surface, it tends to zero when the particle concentration increases. Physically, this means that the particles absorb all the heat flux emerging from the hot surface while settling down under gravity.

The variation in the average Nusselt number $(Nu_h + Nu_c)/2$ with δ_{Ra} near the bifurcation point for different particle volume fractions is shown in figure 5. As expected, $(Nu_h + Nu_c)/2$ increases for all Φ_0 with an increase in δ_{Ra}.

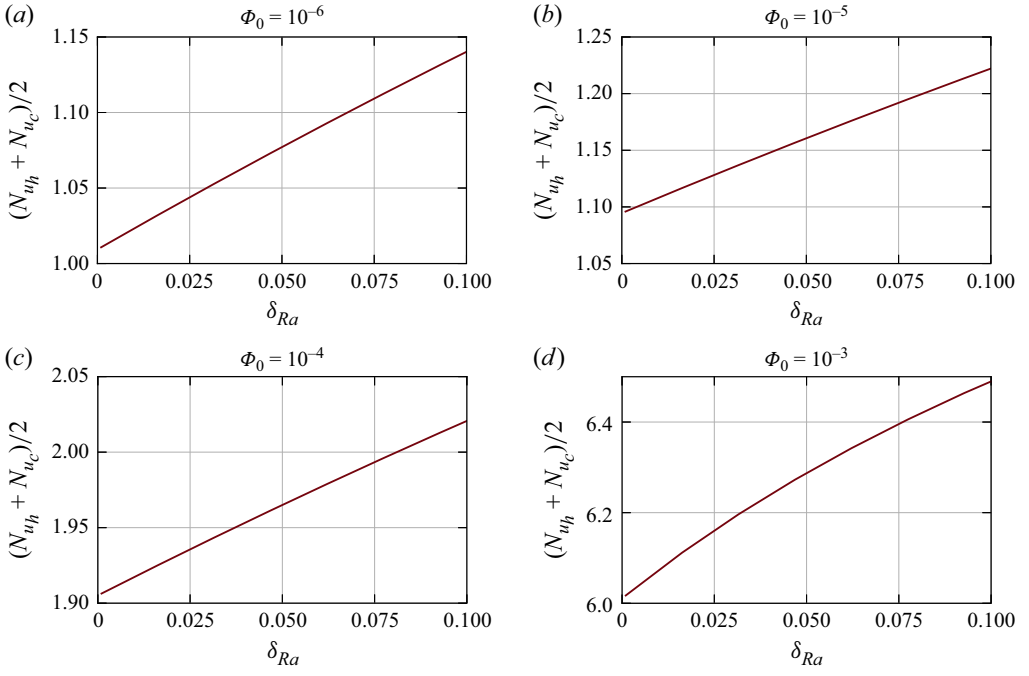

Figure 5. Variation in heat transfer near the bifurcation point at different particle volume fractions and with other parameters kept constant at $\delta = 0.01$, $Re_p = 1$, $R = 800$, $E = 3385$, $\Theta_{pt} = 0$ and $Pr = 0.71$. Here, the heat transfer is measured as the average value of Nu_h and Nu_c.

5.2. *Effect of particle injection temperature*

Figure 6 depicts the effect of particle injection temperature Θ_{pt} on the growth rate c_i, the real part of the Landau constant $\mathrm{Re}\{a_1\}$, equilibrium amplitude A_e, and the ratio of equilibrium amplitude and the square root of growth rate at a fixed particle volume fraction $\Phi_0 = 10^{-4}$, and other parameters kept at $\delta = 0.01$, $\mathrm{Re}_p = 1$, $R = 800$, $E = 3385$ and $Pr = 0.71$. Similar to the non-monotonic effect of Θ_{pt} on the onset of instability (see figure 3), Θ_{pt} shows the non-monotonic effect on the growth rate, the real part of the Landau constant, and the equilibrium amplitude. As described in figure 3, an increase in Θ_{pt} favours stability in the initial part, and the further increase in Θ_{pt} causes flow to favour instability. Hence this explains the decrease in c_i in the initial part, and the increase in c_i in the remaining part of the curves in figure 6(*a*). Figure 6(*b*) shows that for all $\Theta_{pt} \in (-1, 2)$, $\mathrm{Re}\{a_1\} < 0$, and together with $c_i > 0$, the flow exhibits a supercritical pitchfork bifurcation. The equilibrium amplitude A_e has a non-monotonic variation with respect to Θ_{pt}: as Θ_{pt} increases from -1, A_e decreases and reaches a minimum at approximately 1, and again increases. Finally, figure 6(*d*) shows $A_e \sim \sqrt{c_i}$, which is the key underlying assumption while writing the perturbation series of the form given by (4.1).

5.3. *Secondary flow pattern*

Figure 7 shows the variation of perturbation amplitude normalised by the equilibrium amplitude with time for different initial conditions given by (4.11). Due to the supercritical pitchfork bifurcation, for the given control parameter, all the perturbation amplitudes with different initial conditions tend to approach the same equilibrium amplitude as $t \to \infty$. The perturbation series given by (4.1) can be rewritten for the secondary flow $\theta'(x, z, t) = \theta(x, z, t) - \Theta_0(z)$ as

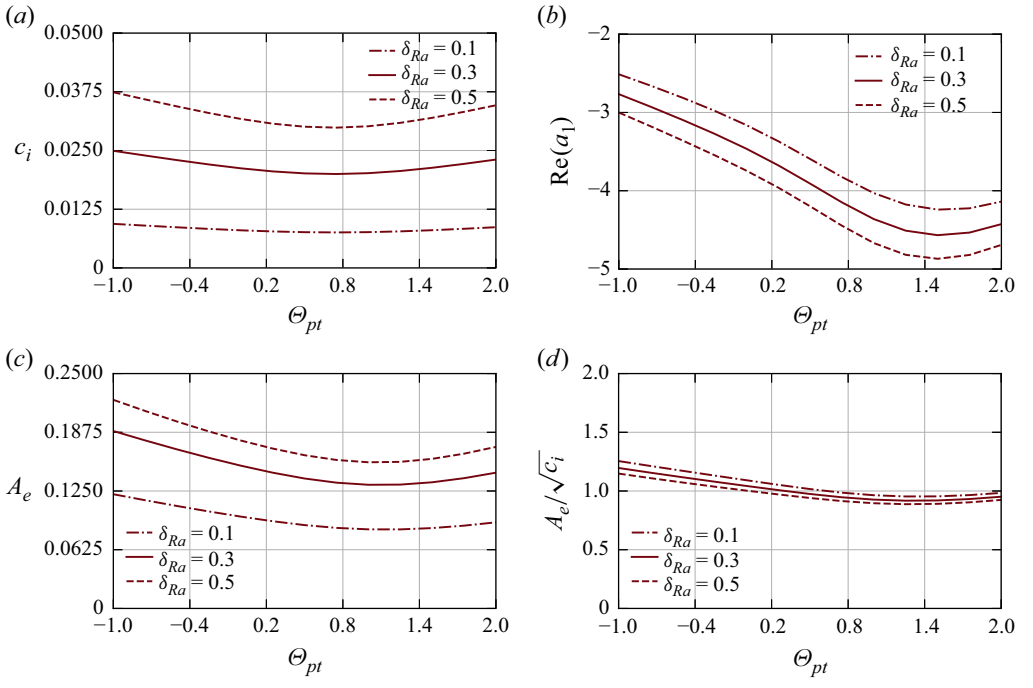

Figure 6. Effect of particle initial temperature Θ_{pt} at $\delta_{Ra} = 0.1$: (*a*) variation of growth rate c_i, (*b*) variation of the real part of the Landau constant Re$\{a_1\}$, (*c*) variation of equilibrium amplitude A_e, and (*d*) variation of the ratio of equilibrium amplitude and the square root of the growth rate. The other parameters are kept at $\delta = 0.01$, $Re_p = 1$, $R = 800$, $E = 3385$, $Pr = 0.71$ and $\Phi_0 = 10^{-4}$.

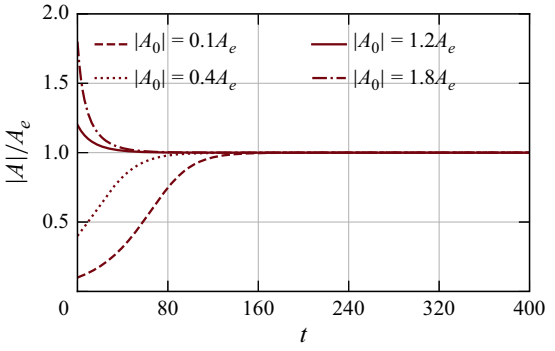

Figure 7. Time history of amplitude function $|A|$ at $\delta_{Ra} = 0.1$ with different initial amplitudes $|A_0|$ at $R = 800$, $E = 3385$, $\Phi_0 = 10^{-4}$, $\Theta_{pt} = 0$, $Re_p = 1$ and $Pr = 0.701$. Here, the amplitude $|A|$ is normalised by the equilibrium amplitude A_e.

$$\theta'(x, z, t) = |A|^2\, \Theta_1(z) + \mathbb{E}^1\left\{A(t)\, \theta_{10}(z) + A\,|A|^2\, \theta_{11}(z)\right\} + \mathbb{E}^2\left\{A^2\, \theta_{20}(z)\right\}, \qquad (5.1)$$

where $A(t)$ is given by (4.15). Using similar expressions for the remaining variables, we obtain the contour plots of secondary flow patterns at $\delta_{Ra} = 0.1$ as shown in figure 8. The secondary flow patterns obtained from the linear stability are shown in the left-hand column, and those obtained from the nonlinear stability analysis are shown in the right-hand column. Due to the presence of particles, the top–bottom symmetry is absent even in the contours obtained from the linear stability analysis. The velocity

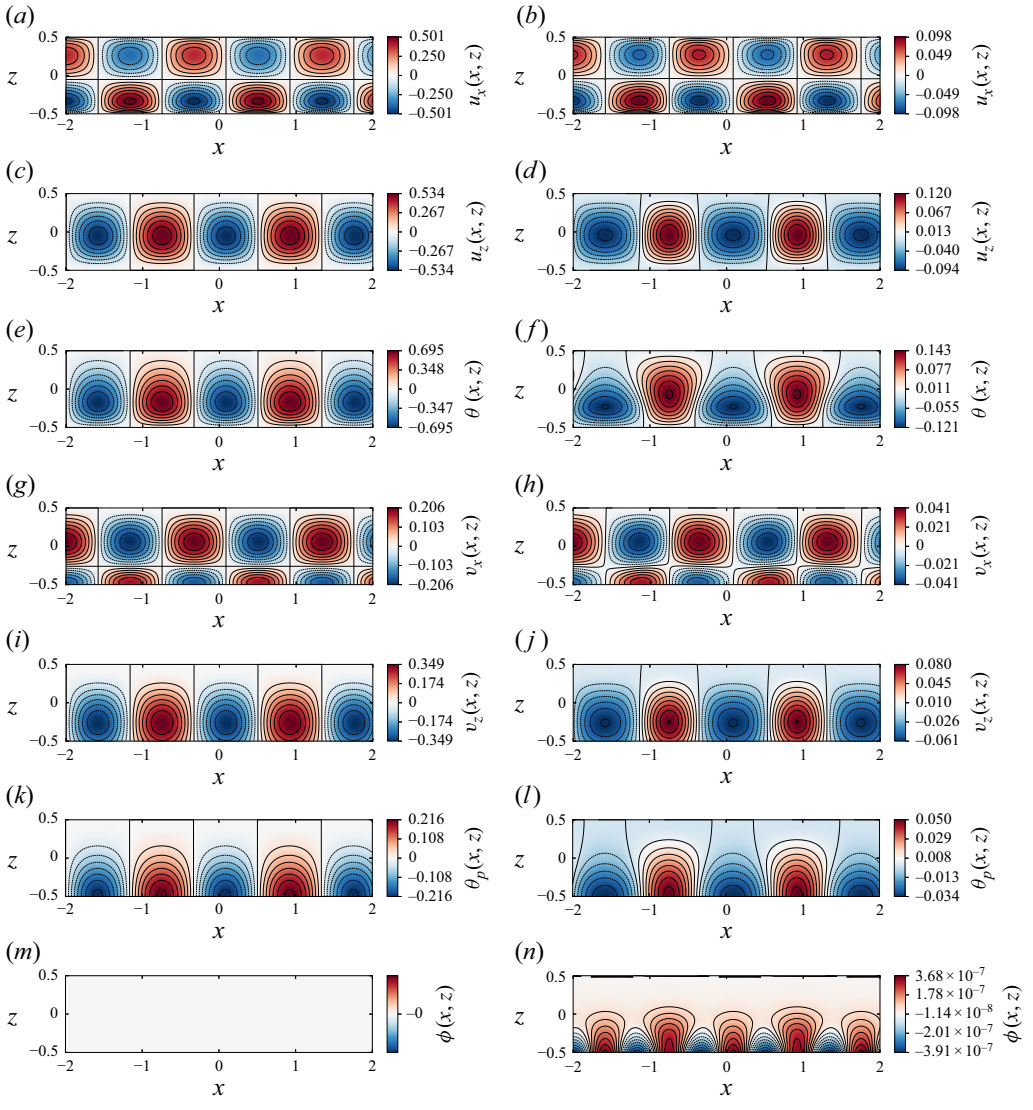

Figure 8. Secondary flow pattern obtained for particle-laden Rayleigh–Bénard convection: (*a*,*c*,*e*,*g*,*i*,*k*,*m*) the linear analysis, (*b*,*d*,*f*,*h*,*j*,*l*,*n*) the nonlinear analysis, at reduced Rayleigh number $\delta_{Ra} = 0.1$, with critical wavenumber $k_c \approx 3.77$, and other parameters $R = 800$, $E = 3385$, $\Phi_0 = 10^{-4}$, $\Theta_{pt} = 0$, $Re_p = 1$ and $Pr = 0.701$.

and temperature profiles for the fluid and particles are qualitatively different due to the momentum and thermal inertia of the particles. It is expected that the distortion of the flow patterns increases with an increase in δ_{Ra} due to a corresponding increase in the equilibrium amplitude. The width of the contour corresponding to the vertical component of velocity u_z is larger for negative values than for positive values. Moreover, at a steady state, the net mass flux across any horizontal plane must be zero to satisfy the continuity equation. Hence the magnitude of the vertical component of velocity in upward flow regions should be higher than that in downward flow.

From the linear stability analysis, we showed that the perturbations in particle volume fractions and divergence of particle velocity field are always zero in the domain (see § A.6). However, when the perturbations are finite, the contribution from the nonlinear terms gives

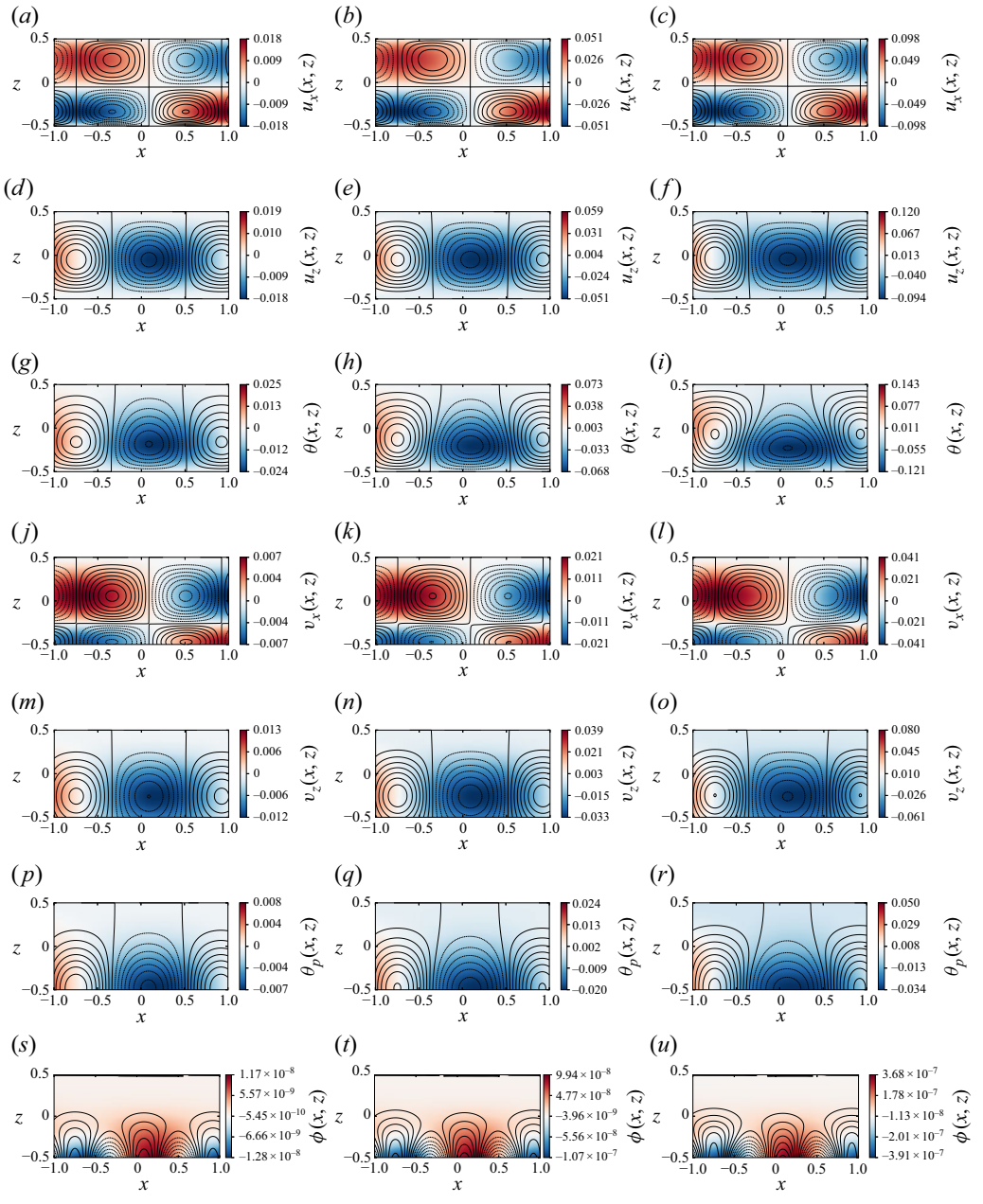

Figure 9. Secondary flow pattern obtained for particle-laden Rayleigh–Bénard convection at (*a*,*d*,*g*,*j*,*m*,*p*,*s*) $t = 20$, (*b*,*e*,*h*,*k*,*n*,*q*,*t*) $t = 60$ and (*c*,*f*,*i*,*l*,*o*,*r*,*u*) $t = 320$, for reduced Rayleigh number $\delta_{Ra} = 0.1$, with critical wavenumber $k_c \approx 3.77$, and other parameters fixed at $R = 800$, $E = 3385$, $\Phi_0 = 10^{-4}$, $\Theta_{pt} = 0$, $Re_p = 1$, $Pr = 0.701$, and the initial amplitude A_0 is taken as $0.1A_e$.

a non-zero distortion function Φ_1, and the second harmonic function $\mathbb{E}^2$, which results in the tendency of particles to become spatially non-uniform as shown in figure 8(*n*). The time evolution of the secondary flow pattern obtained from the present weakly nonlinear analysis before reaching a steady state is shown in figure 9. As shown in figure 7, for initial amplitudes close to zero, the growth amplitude A in time is approximately exponential with

negligible effect of nonlinear terms. However, as time progresses ($t \gtrsim 80$), the nonlinear terms become significant and saturate the exponential growth, leading to a steady-state solution. Here, there is no oscillating solution for this particle-laden Rayleigh–Bénard system, because we observed that $c_r = 0$ always for the most unstable mode, which is also reported in the previous work by Prakhar & Prosperetti (2021). Hence the right-hand panels in figure 9 show the steady-state secondary flow patterns, which are exactly the same as the right-hand panels in figure 8.

6. Conclusions

In this work, we have performed a weakly nonlinear stability analysis of particle-laden Rayleigh–Bénard convection. We assume the particles to be initially uniformly distributed in space and moving with the settling velocity. At the top cold surface, new particles are injected at a uniform particle volume fraction with their terminal velocity, and settled particles at the bottom hot surface are collected. First, using the linear stability, we show that for a given particle size δ, initial temperature Θ_{pt} and particle Reynolds number Re_p, the critical Rayleigh number Ra_c significantly increases with an increase in particle volume fraction Φ_0, whereas the initial particle temperature Θ_{pt} significantly affects the base-state temperature profile and has a non-monotonic effect on Ra_c with the maximum at $\Theta_{pt} \sim 1$.

We derived a Landau equation to study the evolution of the unstable modes in the weakly nonlinear regime in the vicinity of the critical point. In particular, we show that the growth rate reduces with an increase in particle volume fraction. We note that the Landau constant satisfies $\mathrm{Re}\{a_1\} < 0$ for all Φ_0, and together with $c_i > 0$, it leads to a supercritical pitchfork bifurcation with an equilibrium amplitude $A_e = \sqrt{-k_c c_i / \mathrm{Re}\{a_1\}}$. The amplitude A_e reduces with an increase in Φ_0.

Further, at steady state, the Nusselt numbers at the cold and hot surfaces are not equal, like in a single-phase Rayleigh–Bénard convection. This difference in Nusselt numbers at the cold and hot surfaces is exactly balanced by the net sensible heat flux convected by the particles; thus with an increase in Φ_0, the difference in the Nusselt numbers at cold and hot surfaces increases. However, c_i, $\mathrm{Re}\{a_1\}$ and A_e have a non-monotonic dependence on Θ_{pt}. Moreover, for the entire range of values for Θ_{pt} considered in the present work, the analysis showed the supercritical bifurcation for the flow.

Finally, we have analysed the variation in the secondary flow pattern due to the nonlinear interactions of different harmonics. Unlike in single-phase convection, particle-laden Rayleigh–Bénard convection does not show top–bottom symmetry due to the directional settling of the particles under gravity, even in the linear regime. The nonlinear interaction of the fundamental modes generates Reynolds stress or distortion of the base-state temperature and particle volume fraction fields. Interestingly, we observe local clustering of particles due to these nonlinear interactions of fundamental modes. We note that the linear stability analysis does not show particle clustering (see Prakhar & Prosperetti 2021).

Declaration of interests. The authors report no conflict of interest.

Appendix A

A.1. *Linear disturbance equations*

Substitution of the normal modes for all the dependent variables into the linearised governing equations (3.14)–(3.21) leads to a system of linear ordinary differential equations. The resulting equations are represented in the linear operator form as

$$\mathscr{L}_0\big(k,\,\hat{u}_x,\,\hat{u}_z\big)=\mathrm{i}k\hat{u}_x+\frac{\mathrm{d}\hat{u}_z}{\mathrm{d}z}=0, \tag{A1}$$

$$\begin{aligned}&\mathscr{L}_x\big(k,\,c,\,\hat{u}_x,\,\hat{p},\,\hat{v}_x,\,\Phi_0,\,Ra,\,Pr,\,R,\,St_m\big)\\&\quad=\mathrm{i}ck\hat{u}_x+\sqrt{\frac{Pr}{Ra}}\left(\frac{\mathrm{d}^2}{\mathrm{d}z^2}-k^2\right)\hat{u}_x-\mathrm{i}k\hat{p}-\left(\frac{\Phi_0 R}{St_m}\right)\big(\hat{u}_x-\hat{v}_x\big)=0,\end{aligned} \tag{A2}$$

$$\begin{aligned}&\mathscr{L}_z\big(k,\,c,\,\hat{u}_z,\,\hat{p},\,\hat{\theta},\,\hat{v}_z,\,\hat{\phi},\,v_0,\,\Phi_0,\,Ra,\,Pr,\,R,\,St_m\big)\\&\quad=\mathrm{i}ck\hat{u}_z+\sqrt{\frac{Pr}{Ra}}\left(\frac{\mathrm{d}^2}{\mathrm{d}z^2}-k^2\right)\hat{u}_z-\frac{\mathrm{d}\hat{p}}{\mathrm{d}z}+\hat{\theta}-\left(\frac{\Phi_0 R}{St_m}\right)\big(\hat{u}_z-\hat{v}_z\big)-\left(\frac{Rv_0}{St_m}\right)\hat{\phi}=0,\end{aligned} \tag{A3}$$

$$\begin{aligned}&\mathscr{L}_\theta\big(k,\,c,\,\hat{u}_z,\,\hat{\theta},\,\hat{\theta}_p,\,\hat{\phi},\,\Theta_0,\,\Theta_{p0},\,\Phi_0,\,Ra,\,Pr,\,E,\,St_{th}\big)\\&\quad=\mathrm{i}ck\hat{\theta}+\frac{1}{\sqrt{RaPr}}\left(\frac{\mathrm{d}^2}{\mathrm{d}z^2}-k^2\right)\hat{\theta}-\frac{\mathrm{d}\Theta_0}{\mathrm{d}z}\hat{u}_z-\frac{E\Phi_0}{St_{th}}\big(\hat{\theta}-\hat{\theta}_p\big)-\frac{E\big(\Theta_0-\Theta_{p0}\big)}{St_{th}}\hat{\phi}=0,\end{aligned} \tag{A4}$$

$$\mathscr{L}_\phi\big(k,\,c,\,\hat{v}_x,\,\hat{v}_z,\,v_0,\,\Phi_0\big)=\mathrm{i}ck\hat{\phi}-\Phi_0\left(\mathrm{i}k\hat{v}_x+\frac{\mathrm{d}\hat{v}_z}{\mathrm{d}z}\right)+v_0\frac{\mathrm{d}\hat{\phi}}{\mathrm{d}z}=0, \tag{A5}$$

$$\mathscr{L}_{px}\big(k,\,c,\,\hat{u}_x,\,\hat{v}_x,\,v_0,\,St_m\big)=\mathrm{i}ck\hat{v}_x+v_0\frac{\mathrm{d}\hat{v}_x}{\mathrm{d}z}+\frac{\hat{u}_x-\hat{v}_x}{St_m}=0, \tag{A6}$$

$$\mathscr{L}_{pz}\big(k,\,c,\,\hat{u}_z,\,\hat{v}_z,\,v_0,\,St_m\big)=\mathrm{i}ck\hat{v}_z+v_0\frac{\mathrm{d}\hat{v}_z}{\mathrm{d}z}+\frac{\hat{u}_z-\hat{v}_z}{St_m}=0, \tag{A7}$$

$$\mathscr{L}_{p\theta}\big(k,\,c,\,\hat{\theta},\,\hat{v}_z,\,\hat{\theta}_p,\,v_0,\,\Theta_{p0},\,St_{th}\big)=\mathrm{i}ck\hat{\theta}_p+v_0\frac{\mathrm{d}\hat{\theta}_p}{\mathrm{d}z}+\frac{\hat{\theta}-\hat{\theta}_p}{St_{th}}-\frac{\mathrm{d}\Theta_{p0}}{\mathrm{d}z}\hat{v}_z=0 \tag{A8}$$

for $z\in(-1/2,\,1/2)$.

A.2. *Equations at different hormonic components*

The equations for the harmonic $\mathbb{E}^0$ are given as

$$\begin{aligned}&\mathcal{L}_z\big(P_0,\,\Theta_0,\,v_0,\,\Phi_0,\,R,\,St_m\big)+c_i\,|B|^2\left\{\mathcal{L}_z(P_1,\,\Theta_1,\,-V_1,\,\Phi_0,\,R,\,St_m)+\frac{Rv_0}{St_m}\Phi_1\right\}\\&\quad+c_i\,|B|^2\left\{2\frac{\mathrm{d}}{\mathrm{d}z}\,(\tilde{u}_{z10}u_{z10})+\frac{R}{St_m}\big\{\phi_{10}(\tilde{u}_{z10}-\tilde{v}_{z10})+\tilde{\phi}_{10}(u_{z10}-v_{z10})\big\}\right\}=\mathcal{O}\big(c_i^2\big),\end{aligned} \tag{A9}$$

$$\begin{aligned}&\mathcal{L}_\theta\big(\Theta_0,\,\Theta_{p0},\,\Phi_0,\,Ra,\,Pr,\,E,\,St_{th}\big)\\&\quad+c_i\,|B|^2\left\{\mathcal{L}_\theta\big(\Theta_1,\,\Theta_{p1},\,\Phi_0,\,Ra,\,Pr,\,E,\,St_{th}\big)-\frac{E\big(\Theta_0-\Theta_{p0}\big)}{St_{th}}\Phi_1\right\}\\&\quad-c_i\,|B|^2\left\{\frac{\mathrm{d}}{\mathrm{d}z}\left(\tilde{\theta}_{10}u_{z10}+\theta_{10}\tilde{u}_{z10}\right)+\frac{E}{St_{th}}\Big(\phi_{10}\big(\tilde{\theta}_{10}-\tilde{\theta}_{p10}\big)+\tilde{\phi}_{10}\big(\theta_{10}-\theta_{p10}\big)\Big)\right\}\\&\quad=\mathcal{O}\big(c_i^2\big),\end{aligned} \tag{A10}$$

$$c_i\,|B|^2\left\{\Phi_0\frac{\mathrm{d}V_1}{\mathrm{d}z}-v_0\frac{\mathrm{d}\Phi_1}{\mathrm{d}z}+\frac{\mathrm{d}}{\mathrm{d}z}\left(\phi_{10}\tilde{v}_{z10}\right)+\frac{\mathrm{d}}{\mathrm{d}z}\left(\tilde{\phi}_{10}v_{z10}\right)\right\}=\mathcal{O}\left(c_i^2\right), \tag{A11}$$

$$c_i\,|B|^2\left\{\left(v_0\frac{\mathrm{d}V_1}{\mathrm{d}z}-\frac{V_1}{St_m}\right)+\mathrm{i}k_c(v_{x10}\tilde{v}_{z10}-\tilde{v}_{x10}v_{z10})-\frac{\mathrm{d}}{\mathrm{d}z}\left(v_{z10}\tilde{v}_{z10}\right)\right\}=\mathcal{O}\left(c_i^2\right), \tag{A12}$$

$$\begin{aligned}&\mathcal{L}_{p\theta}\left(\Theta_0,\,\Theta_{p0},\,v_0,\,St_{th}\right)+c_i\,|B|^2\left\{\mathcal{L}_{p\theta}\left(\Theta_1,\,\Theta_{p1},\,v_0,\,St_{th}\right)-V_1\frac{\mathrm{d}\Theta_{p0}}{\mathrm{d}z}\right\}\\&\quad-c_i|B|^2\left\{v_{z10}\frac{\mathrm{d}\tilde{\theta}_{p10}}{\mathrm{d}z}+\tilde{v}_{z10}\frac{\mathrm{d}\theta_{p10}}{\mathrm{d}z}+\mathrm{i}k_c\left(\tilde{v}_{x10}\theta_{p10}-v_{x10}\tilde{\theta}_{p10}\right)\right\}=\mathcal{O}\left(c_i^2\right)\end{aligned} \tag{A13}$$

for $z\in(-1/2,\,1/2)$, where the operators $\mathcal{L}_z$, $\mathcal{L}_\theta$ and $\mathcal{L}_{p\theta}$ are given by (3.1), (3.2) and (3.3), respectively. The boundary conditions for Θ_1, V_1, Θ_{p1} and Φ_1 are given by

$$\left.\begin{array}{ll}\text{at } z=-1/2, & \Theta_1=0,\\ \text{at } z=1/2, & \Theta_1=V_1=\Theta_{p1}=\Phi_1=0.\end{array}\right\} \tag{A14}$$

Similarly, the equations for the harmonic $\mathbb{E}^1$ are given by

$$(c_i)^{1/2}B\,\mathscr{L}_0(k_c,\,u_{x10},\,u_{z10})+(c_i)^{3/2}B\,|B|^2\,\mathscr{L}_0(k_c,\,u_{x11},\,u_{z11})=\mathcal{O}\left(c_i^{5/2}\right), \tag{A15}$$

$$\begin{aligned}&(c_i)^{1/2}B\,\mathscr{L}_x(k_c,\,c,\,u_{x10},\,p_{10},\,v_{x10},\,\Phi_0,\,Ra,\,Pr,\,R,\,St_m)\\&\quad+(c_i)^{3/2}B\,|B|^2\,\mathscr{L}_x(k_c,\,c,\,u_{x11},\,p_{11},\,v_{x11},\,\Phi_0,\,Ra,\,Pr,\,R,\,St_m)\\&\quad-(c_i)^{3/2}\left(B\,|B|^2\mathcal{G}_x+\left\{\frac{\mathrm{d}B}{\mathrm{d}\tau}-k_cB\right\}u_{x10}\right)=\mathcal{O}\left(c_i^{5/2}\right),\end{aligned} \tag{A16}$$

$$\begin{aligned}&(c_i)^{1/2}B\,\mathscr{L}_z(k_c,\,c,\,u_{z10},\,p_{10},\,\theta_{10},\,v_{z10},\,\phi_{10},\,v_0,\,\Phi_0,\,Ra,\,Pr,\,R,\,St_m)\\&\quad+(c_i)^{3/2}B\,|B|^2\,\mathscr{L}_z(k_c,\,c,\,u_{z11},\,p_{11},\,\theta_{11},\,v_{z11},\,\phi_{11},\,v_0,\,\Phi_0,\,Ra,\,Pr,\,R,\,St_m)\\&\quad-(c_i)^{3/2}\left(B\,|B|^2\mathcal{G}_z+\left\{\frac{\mathrm{d}B}{\mathrm{d}\tau}-k_cB\right\}u_{z10}\right)=\mathcal{O}\left(c_i^{5/2}\right),\end{aligned} \tag{A17}$$

$$\begin{aligned}&(c_i)^{1/2}B\,\mathscr{L}_\theta\left(k_c,\,c,\,u_{z10},\,\theta_{10},\,\theta_{p10},\,\phi_{10},\,\Theta_0,\,\Theta_{p0},\,\Phi_0,\,Ra,\,Pr,\,E,\,St_{th}\right)\\&\quad+(c_i)^{3/2}B\,|B|^2\,\mathscr{L}_\theta\left(k_c,\,c,\,u_{z11},\,\theta_{11},\,\theta_{p11},\,\phi_{11},\,\Theta_0,\,\Theta_{p0},\,\Phi_0,\,Ra,\,Pr,\,E,\,St_{th}\right)\\&\quad-(c_i)^{3/2}\left(B\,|B|^2\mathcal{G}_\theta+\left\{\frac{\mathrm{d}B}{\mathrm{d}\tau}-k_cB\right\}\theta_{10}\right)=\mathcal{O}\left(c_i^{5/2}\right),\end{aligned} \tag{A18}$$

$$\begin{aligned}&(c_i)^{1/2}B\mathscr{L}_\phi(k_c,\,c,\,v_{x10},\,v_{z10},\,\phi_{10},\,v_0,\,\Phi_0)\\&\quad+(c_i)^{3/2}B\,|B|^2\,\mathscr{L}_\phi(k_c,\,c,\,v_{x11},\,v_{z11},\,\phi_{11},\,v_0,\,\Phi_0)\\&\quad-(c_i)^{3/2}\left(B\,|B|^2\mathcal{G}_\phi+\left\{\frac{\mathrm{d}B}{\mathrm{d}\tau}-k_cB\right\}\phi_{10}\right)=\mathcal{O}\left(c_i^{5/2}\right),\end{aligned} \tag{A19}$$

$$\begin{aligned}&(c_i)^{1/2}\mathscr{L}_{px}(k_c,\,c,\,u_{x10},\,v_{x10},\,v_0,\,St_m)+(c_i)^{3/2}B|B|^2\,\mathscr{L}_{px}(k_c,\,c,\,u_{x11},\,v_{x11},\,v_0,\,St_m)\\&\quad-(c_i)^{3/2}\left(B\,|B|^2\mathcal{G}_{px}+\left\{\frac{\mathrm{d}B}{\mathrm{d}\tau}-k_cB\right\}v_{x10}\right)=\mathcal{O}\left(c_i^{5/2}\right),\end{aligned} \tag{A20}$$

$$\begin{aligned}&(c_i)^{1/2}B\mathscr{L}_{pz}(k_c,\,c,\,u_{z10},\,v_{z10},\,v_0,\,St_m)+(c_i)^{3/2}B|B|^2\,\mathscr{L}_{pz}(k_c,\,c,\,u_{z11},\,v_{z11},\,v_0,\,St_m)\\&\quad-(c_i)^{3/2}\left(B\,|B|^2\mathcal{G}_{pz}+\left\{\frac{\mathrm{d}B}{\mathrm{d}\tau}-k_cB\right\}v_{z10}\right)=\mathcal{O}\left(c_i^{5/2}\right),\end{aligned} \tag{A21}$$

$$(c_i)^{1/2} B \mathscr{L}_{p\theta}\left(k_c, c, \theta_{10}, v_{z10}, \theta_{p10}, v_0, \Theta_{p0}, St_{th}\right) + (c_i)^{3/2} B\,|B|^2\,\mathscr{L}_{p\theta}\left(k_c, c, \theta_{11}, v_{z11}, \theta_{p11}, v_0, \Theta_{p0}, St_{th}\right) - (c_i)^{3/2}\left(B\,|B|^2 \mathcal{G}_{p\theta} + \left\{\frac{\mathrm{d}B}{\mathrm{d}\tau} - k_c B\right\}\theta_{p10}\right) = \mathcal{O}\left(c_i^{5/2}\right) \tag{A22}$$

for $z \in (-1/2, 1/2)$, where the operators $\mathscr{L}_0$, $\mathscr{L}_x$, $\mathscr{L}_z$, $\mathscr{L}_\theta$, $\mathscr{L}_\phi$, $\mathscr{L}_{px}$, $\mathscr{L}_{pz}$ and $\mathscr{L}_{p\theta}$ are the linear stability operators given by (A1)–(A8) with boundary conditions given by (3.23) for both $(u_{x10}, u_{z10}, \theta_{10}, v_{x10}, v_{z10}, \theta_{p10}, \phi_{10})$ and $(u_{x11}, u_{z11}, \theta_{11}, v_{x11}, v_{z11}, \theta_{p11}, \phi_{11})$. Here, the scalar functions $\mathcal{G}_x$, $\mathcal{G}_z$, $\mathcal{G}_\theta$, $\mathcal{G}_{px}$, $\mathcal{G}_{pz}$, $\mathcal{G}_\phi$ and $\mathcal{G}_{p\theta}$ are given by (A31)–(A37) defined in § A.3.

The equations for the harmonic $\mathbb{E}^2$ are given by

$$c_i B^2\,\mathscr{L}_0(2k_c, u_{x20}, u_{z20}) = \mathcal{O}\left(c_i^2\right), \tag{A23}$$

$$c_i B^2\,\mathscr{L}_x(2k_c, u_{x20}, p_{20}, v_{x20}, \Phi_0, Ra, Pr, R, St_m) - c_i B^2\left\{u_{z10}\frac{\mathrm{d}u_{x10}}{\mathrm{d}z} - u_{x10}\frac{\mathrm{d}u_{z10}}{\mathrm{d}z} + \frac{R\phi_{10}}{St_m}(u_{x10} - v_{x10})\right\} = \mathcal{O}\left(c_i^2\right), \tag{A24}$$

$$c_i B^2\left\{\mathscr{L}_z(2k_c, c, u_{z20}, p_{20}, \theta_{20}, v_{z20}, \Phi_0, Ra, Pr, R, St_m) - \frac{R\phi_{10}}{St_m}(u_{z10} - u_{x10})\right\} = \mathcal{O}\left(c_i^2\right), \tag{A25}$$

$$c_i B^2\,\mathscr{L}_\theta\left(2k_c, c, u_{z20}, \theta_{20}, \theta_{p20}, \phi_{20}, \Theta_0, \Theta_{p0}, \Phi_0, Ra, Pr, E, St_{th}\right) - c_i B^2\left\{u_{z10}\frac{\mathrm{d}\theta_{10}}{\mathrm{d}z} - \theta_{10}\frac{\mathrm{d}u_{z10}}{\mathrm{d}z} + \frac{E\phi_{10}}{St_{th}}\left(\theta_{10} - \theta_{p10}\right)\right\} = \mathcal{O}\left(c_i^2\right), \tag{A26}$$

$$c_i B^2\,\mathscr{L}_\phi(2k_c, c, v_{x20}, v_{z20}, \phi_{20}, v_0, \Phi_0) - c_i B^2\left\{2\mathrm{i}k_c\phi_{10}v_{x10} + \frac{\mathrm{d}}{\mathrm{d}z}\left(\phi_{10}v_{z10}\right)\right\} = \mathcal{O}\left(c_i^2\right), \tag{A27}$$

$$c_i B^2\left\{\mathscr{L}_{px}(2k_c, c, u_{x20}, v_{x20}, v_0, St_m) - \left(\mathrm{i}k_c v_{x10}^2 + v_{z10}\frac{\mathrm{d}v_{x10}}{\mathrm{d}z}\right)\right\} = \mathcal{O}\left(c_i^2\right), \tag{A28}$$

$$c_i B^2\left\{\mathscr{L}_{pz}(2k_c, c, u_{z20}, v_{z20}, v_0, St_m) - \left(\mathrm{i}k_c v_{x10}v_{z10} + v_{z10}\frac{\mathrm{d}v_{z10}}{\mathrm{d}z}\right)\right\} = \mathcal{O}\left(c_i^2\right), \tag{A29}$$

$$c_i B^2\left\{\mathscr{L}_{p\theta}\left(2k_c, c, \theta_{20}, v_{z20}, \theta_{p20}, v_0, \Theta_{p0}, St_{th}\right) - \left(\mathrm{i}k_c v_{x10}\theta_{p10} + v_{z10}\frac{\mathrm{d}\theta_{p10}}{\mathrm{d}z}\right)\right\} = \mathcal{O}\left(c_i^2\right) \tag{A30}$$

for $z \in (-1/2, 1/2)$, and the boundary conditions are similar to (3.23). Here, $\sim$ represents the complex conjugate.

A.3. *Scalar functions*

In the derivation of the Landau equation, the following scalar functions emerge due to the nonlinear interaction of different modes:

$$\mathcal{G}_x = \tilde{u}_{z10}\frac{\mathrm{d}u_{x20}}{\mathrm{d}z} + u_{z20}\frac{\mathrm{d}\tilde{u}_{x10}}{\mathrm{d}z} - \mathrm{i}k_c u_{x20}\tilde{u}_{x10} + 2u_{x20}\frac{\mathrm{d}\tilde{u}_{z10}}{\mathrm{d}z} + \frac{R}{St_m}\big(\Phi_1\{u_{x10} - v_{x10}\} + \phi_{20}\{\tilde{u}_{x10} - \tilde{v}_{x10}\} + \tilde{\phi}_{10}\{u_{x20} - v_{x20}\}\big), \tag{A31}$$

$$\mathcal{G}_z = \tilde{u}_{z10}\frac{\mathrm{d}u_{z20}}{\mathrm{d}z} + u_{z20}\frac{\mathrm{d}\tilde{u}_{z10}}{\mathrm{d}z} - \mathrm{i}k_c u_{x20}\tilde{u}_{z10} + 2u_{z20}\frac{\mathrm{d}\tilde{u}_{z10}}{\mathrm{d}z} + \frac{R}{St_m}\big(\Phi_1\{u_{z10} - v_{z10}\} + \phi_{20}\{\tilde{u}_{z10} - \tilde{v}_{z10}\} + \tilde{\phi}_{10}\{u_{z20} - v_{z20}\} - \phi_{10}V_1\big), \tag{A32}$$

$$\mathcal{G}_\theta = \tilde{u}_{z10}\frac{\mathrm{d}\theta_{20}}{\mathrm{d}z} + u_{z20}\frac{\mathrm{d}\tilde{\theta}_{10}}{\mathrm{d}z} - \mathrm{i}k_c u_{x20}\tilde{\theta}_{10} + 2\theta_{20}\frac{\mathrm{d}\tilde{u}_{z10}}{\mathrm{d}z} + u_{z10}\frac{\mathrm{d}\Theta_1}{\mathrm{d}z} + \frac{E}{St_{th}}\big(\phi_{10}(\Theta_1 - \Theta_{p1}) + \tilde{\phi}_{10}(\theta_{20} - \theta_{p20}) + \Phi_1(\theta_{10} - \theta_{p10}) + \phi_{20}(\tilde{\theta}_{10} - \tilde{\theta}_{p10})\big), \tag{A33}$$

$$\mathcal{G}_\phi = \frac{\mathrm{d}}{\mathrm{d}z}\big(\tilde{v}_{z10}\phi_{20}\big) + \frac{\mathrm{d}}{\mathrm{d}z}\big(v_{z20}\tilde{\phi}_{10}\big) + \mathrm{i}k_c\big(v_{x20}\tilde{\phi}_{10} + \tilde{v}_{x10}\phi_{20} + \Phi_1 v_{x10}\big) + \frac{\mathrm{d}}{\mathrm{d}z}(\Phi_1 v_{z10}) + \frac{\mathrm{d}}{\mathrm{d}z}(\phi_{10}V_1), \tag{A34}$$

$$\mathcal{G}_{px} = \tilde{v}_{z10}\frac{\mathrm{d}v_{x20}}{\mathrm{d}z} + v_{z20}\frac{\mathrm{d}\tilde{v}_{x10}}{\mathrm{d}z} - \mathrm{i}k_c v_{x20}\tilde{v}_{x10} + 2\mathrm{i}k_c\tilde{v}_{x10}v_{x20} + V_1\frac{\mathrm{d}v_{x10}}{\mathrm{d}z}, \tag{A35}$$

$$\mathcal{G}_{pz} = \tilde{v}_{z10}\frac{\mathrm{d}v_{z20}}{\mathrm{d}z} + v_{z20}\frac{\mathrm{d}\tilde{v}_{z10}}{\mathrm{d}z} - \mathrm{i}k_c v_{x20}\tilde{v}_{z10} + 2\mathrm{i}k_c\tilde{v}_{x10}v_{z20} + \frac{\mathrm{d}}{\mathrm{d}z}(V_1 v_{z10}), \tag{A36}$$

$$\mathcal{G}_{p\theta} = \tilde{v}_{z10}\frac{\mathrm{d}\theta_{p20}}{\mathrm{d}z} + v_{z20}\frac{\mathrm{d}\tilde{\theta}_{p10}}{\mathrm{d}z} - \mathrm{i}k_c v_{x20}\tilde{\theta}_{p10} + 2\mathrm{i}k_c\tilde{v}_{x10}\theta_{p20} + V_1\frac{\mathrm{d}\theta_{p10}}{\mathrm{d}z} + v_{z10}\frac{\mathrm{d}\Theta_{p1}}{\mathrm{d}z}. \tag{A37}$$

A.4. *Linear adjoint equations*

The adjoint of the linear operator $\mathscr{L}$ is defined as

$$\big\langle \boldsymbol{X}^\dagger, \mathscr{L}\boldsymbol{X}\big\rangle = \big\langle \mathscr{L}^\dagger\boldsymbol{X}^\dagger, \boldsymbol{X}\big\rangle, \tag{A38}$$

where $\boldsymbol{X}^\dagger$ is the eigenvector corresponding to the adjoint operator $\mathscr{L}^\dagger$. The definition for the inner product used in (A38) for the two real-valued vector functions $\boldsymbol{X}(z) = [x_1 \;\; x_2 \;\; x_3 \;\; x_4 \;\; x_5 \;\; x_6 \;\; x_7 \;\; x_8]^{\mathrm{T}}$ and $\boldsymbol{Y}(z) = [y_1 \;\; y_2 \;\; y_3 \;\; y_4 \;\; y_5 \;\; y_6 \;\; y_7 \;\; y_8]^{\mathrm{T}}$ is given by

$$\langle \boldsymbol{X}, \boldsymbol{Y}\rangle = \int_{z=-1/2}^{1/2} [\boldsymbol{X}]^{\mathrm{T}}\,\boldsymbol{Y}\,\mathrm{d}z = \int_{z=-1/2}^{1/2}\sum_{j=1}^{8} x_j(z)\,y_j(z)\,\mathrm{d}z. \tag{A39}$$

Using the definition for the adjoint in (A38), the adjoint linear system corresponding to the linear stability (A1)–(A8) is given by

$$\mathscr{L}_0^\dagger\big(k_c, \hat{u}_x^\dagger, \hat{u}_z^\dagger\big) = -\mathrm{i}k_c\hat{u}_x^\dagger + \frac{\mathrm{d}\hat{u}_z^\dagger}{\mathrm{d}z} = 0, \tag{A40}$$

$$\mathscr{L}_x^\dagger\big(k_c, c, u_x^\dagger, \hat{p}^\dagger, \hat{v}_x^\dagger, \Phi_0, Ra, Pr, R, St_m\big) = \mathrm{i}ck_c\hat{u}_x^\dagger + \sqrt{\frac{Pr}{Ra}}\left(\frac{\mathrm{d}^2}{\mathrm{d}z^2} - k_c^2\right)\hat{u}_x^\dagger + \mathrm{i}k_c\hat{p}^\dagger - \left(\frac{\Phi_0 R}{St_m}\right)\hat{u}_x^\dagger + \frac{\hat{v}_x^\dagger}{St_m} = 0, \tag{A41}$$

$$\mathscr{L}_z^\dagger\left(k_c, c, u_z^\dagger, \hat{p}^\dagger, \hat{\theta}^\dagger, \hat{v}_z^\dagger, \Theta_0, \Phi_0, Ra, Pr, R, St_m\right)$$
$$= \mathrm{i}ck_c\hat{u}_z^\dagger + \sqrt{\frac{Pr}{Ra}}\left(\frac{\mathrm{d}^2}{\mathrm{d}z^2} - k_c^2\right)\hat{u}_z^\dagger - \frac{\mathrm{d}\hat{p}^\dagger}{\mathrm{d}z} - \frac{\mathrm{d}\Theta_0}{\mathrm{d}z}\hat{\theta}^\dagger - \left(\frac{\Phi_0 R}{St_m}\right)\hat{u}_z^\dagger + \frac{\hat{v}_z^\dagger}{St_m} = 0, \quad \text{(A42)}$$

$$\mathscr{L}_\theta^\dagger\left(k_c, c, \hat{u}_z^\dagger, \hat{\theta}^\dagger, \hat{\theta}_p^\dagger, \Phi_0, Ra, Pr, St_{th}, E\right)$$
$$= \mathrm{i}ck_c\hat{\theta}^\dagger + \frac{1}{\sqrt{RaPr}}\left(\frac{\mathrm{d}^2}{\mathrm{d}z^2} - k_c^2\right)\hat{\theta}^\dagger + \hat{u}_z^\dagger - \frac{E\Phi_0}{St_{th}}\hat{\theta}^\dagger + \frac{\hat{\theta}_p^\dagger}{St_{th}} = 0, \quad \text{(A43)}$$

$$\mathscr{L}_\phi^\dagger\left(k_c, c, \hat{u}_z^\dagger, \hat{\theta}^\dagger, \hat{\phi}^\dagger, \Theta_0, v_0, \Theta_{p0}, St_m, R, St_{th}, E\right)$$
$$= \mathrm{i}ck_c\hat{\phi}^\dagger - v_0\frac{\mathrm{d}\hat{\phi}^\dagger}{\mathrm{d}z} - \frac{Rv_0}{St_m}\hat{u}_z^\dagger - \frac{E\left(\Theta_0 - \Theta_{p0}\right)}{St_{th}}\hat{\theta}^\dagger = 0, \quad \text{(A44)}$$

$$\mathscr{L}_{px}^\dagger\left(k_c, c, \hat{u}_x^\dagger, \hat{v}_x^\dagger, \hat{\phi}^\dagger, v_0, \Phi_0, R, St_m\right)$$
$$= \mathrm{i}ck_c\hat{v}_x^\dagger - v_0\frac{\mathrm{d}\hat{v}_x^\dagger}{\mathrm{d}z} - \frac{\hat{v}_x^\dagger}{St_m} - \mathrm{i}k_c\Phi_0\hat{\phi}^\dagger + \frac{\Phi_0 R}{St_m}\hat{u}_x^\dagger = 0, \quad \text{(A45)}$$

$$\mathscr{L}_{pz}^\dagger\left(k_c, c, \hat{u}_z^\dagger, \hat{v}_z^\dagger, \hat{\theta}_p^\dagger, \hat{\phi}^\dagger, \Theta_0, v_0, \Phi_0, R, St_m\right)$$
$$= \mathrm{i}ck_c\hat{v}_z^\dagger - v_0\frac{\mathrm{d}\hat{v}_z^\dagger}{\mathrm{d}z} - \frac{\hat{v}_z^\dagger}{St_m} + \Phi_0\frac{\mathrm{d}\hat{\phi}^\dagger}{\mathrm{d}z} + \frac{\Phi_0 R}{St_m}\hat{u}_z^\dagger - \frac{\mathrm{d}\Theta_{p0}}{\mathrm{d}z}\hat{\theta}_p^\dagger = 0, \quad \text{(A46)}$$

$$\mathscr{L}_{p\theta}\left(k_c, c, \hat{\theta}^\dagger, \hat{\theta}_p^\dagger, v_0, \Phi_0, E, St_{th}\right) = \mathrm{i}ck_c\hat{\theta}_p^\dagger - v_0\frac{\mathrm{d}\hat{\theta}_p^\dagger}{\mathrm{d}z} - \frac{\hat{\theta}_p^\dagger}{St_{th}} + \frac{E\Phi_0}{St_{th}}\hat{\theta}^\dagger = 0 \quad \text{(A47)}$$

for $z \in (-1/2, 1/2)$ with boundary conditions given by

$$\left.\begin{array}{l} \text{at } z = -1/2, \quad \hat{u}_x^\dagger = \hat{u}_z^\dagger = \hat{\theta}^\dagger = \hat{v}_x^\dagger = \hat{v}_z^\dagger = \hat{\theta}_p^\dagger = \hat{\phi}^\dagger = 0, \\ \text{at } z = 1/2, \quad \hat{u}_x^\dagger = \hat{u}_z^\dagger = \hat{\theta}^\dagger = 0. \end{array}\right\} \quad \text{(A48)}$$

The adjoint eigenfunctions are normalised such that

$$\int_{-1/2}^{1/2}\left(u_{x10}\hat{u}_x^\dagger + u_{z10}\hat{u}_z^\dagger + \theta_{10}\hat{\theta}^\dagger + \phi_{10}\hat{\phi}^\dagger + v_{x10}\hat{v}_x^\dagger + v_{z10}\hat{v}_z^\dagger + \theta_{p10}\hat{\theta}_p^\dagger\right)\mathrm{d}z = 1. \quad \text{(A49)}$$

A.5. *Numerical procedure*

The basic state equations are solved analytically, and the linear and nonlinear stability equations in the present work are solved using the spectral Chebyshev collocation method (Boyd 2001). The underlying system of linear and nonlinear equations, along with the boundary conditions, is transformed into the Chebyshev polynomial domain, i.e. $[-1, 1]$, using the transformation $\xi = 2z$. Here, the continuous variable ξ is discretised onto collocated Gauss–Labatto points ξ_j given by

$$\xi_j = \cos\left(\frac{(j-1)\pi}{N-1}\right), \quad \text{for } j = 1, 2, \ldots, N, \quad \text{(A50)}$$

where $N - 1$ is the degree of the Chebyshev polynomial. All derivatives are obtained using the MATLAB differential matrix suite by Weideman & Reddy (2000). The generalised

eigenvalue problem of the form $\mathbb{A}_d \boldsymbol{q}_d = c\mathbb{B}_d \boldsymbol{q}_d$ is solved using the QZ algorithm (Moler & Stewart 1973) in MATLAB using the `eig` command for the linear stability analysis. Here, $\boldsymbol{q}_d$ is a discretised eigenvector, and $\mathbb{A}_d$ and $\mathbb{B}_d$ are the discretised complex square matrices. The system of adjoint equations of the linear stability problem is solved using a similar spectral method. In nonlinear stability analysis, we need to solve a system of non-homogeneous equations of the form $\mathcal{A}X = b$, here $\mathcal{A} = \mathbb{A}_d - c\mathbb{B}_d$. For the harmonic $\mathbb{E}^2$, the wavenumber k_c is replaced by $2k_c$, and the complex wave speed c of the fundamental harmonic $\mathbb{E}^1$ is not an eigenvalue of this system. Hence the matrix $\mathcal{A} = \mathbb{A}_d - c\mathbb{B}_d$ is non-singular and can be inverted, and gives a unique solution for the harmonic $\mathbb{E}^2$. Similarly, the distortion functions also result in a system of non-singular, non-homogeneous equations, which are solved in a similar manner. For the harmonic $\mathbb{E}^1$ at $\mathcal{O}(c_i^{3/2})$, the system $\mathcal{A}X_{11} = b$ turns out to be singular, and the existence of the solution is guaranteed by applying the Fredholm alternative. However, the solution X_{11} is non-unique; hence one of the solutions is obtained using the singular value decomposition (SVD) built into the MATLAB software. All the integrals required for obtaining the Landau constant a_1 and normalisation are evaluated using the Gauss–Chebyshev quadrature formula.

The numerical code developed for solving the linear stability equations is validated by comparing the results with earlier work by Prakhar & Prosperetti (2021). The results generated by the code are in excellent agreement with the published results. For the nonlinear stability calculations, the results remain consistent when the order of the polynomial N is 50 or more (shown in table 1). Therefore, for all the computations, the polynomial order is taken to be 50.

A.6. *Solution to linearised particle concentration*

From the above, the linearised equations for the particle volume fraction and the divergence of the particle velocity field for the particle-laden Rayleigh–Bénard convection are given by

$$\frac{\partial \phi'}{\partial t} = v_0 \frac{\partial \phi'}{\partial z} - \Phi_0 \left(\frac{\partial v_x'}{\partial x} + \frac{\partial v_z'}{\partial z} \right), \tag{A51}$$

$$\frac{\partial}{\partial t}\left(\frac{\partial v_x'}{\partial x} + \frac{\partial v_z'}{\partial z} \right) = v_0 \frac{\partial}{\partial z}\left(\frac{\partial v_x'}{\partial x} + \frac{\partial v_z'}{\partial z} \right) - \frac{1}{St_m}\left(\frac{\partial v_x'}{\partial x} + \frac{\partial v_z'}{\partial z} \right) \tag{A52}$$

for $(x, z, t) \in \{\mathbb{R} \times (-1/2, 1/2) \times (0, \infty)\}$. Since the above equations are linear, and the coefficients are only functions of spatial variables (x, z), the general solution can be expressed as

$$\phi' = f(x, z)\, e^{\alpha t}, \tag{A53}$$

$$\frac{\partial v_x'}{\partial x} + \frac{\partial v_z'}{\partial z} = g(x, z)\, e^{\alpha t}, \tag{A54}$$

where $\alpha \in \mathbb{C}$ in general. By substituting (A53)–(A54) in (A51)–(A52), we obtain

$$\left(\frac{\partial v_x'}{\partial x} + \frac{\partial v_z'}{\partial z} \right)(x, z, t) = f_t(x) \exp\left\{ -\left(\alpha + \frac{1}{St_m} \right) \frac{1/2 - z}{v_0} \right\} e^{\alpha t}, \tag{A55}$$

$$\phi'(x, z, t) = \left(g_t(x) - f_t(x) \left(\frac{\Phi_0 St_m}{v_0} \right) \left[1 - \exp\left\{ -\frac{1}{St_m} \frac{1/2 - z}{v_0} \right\} \right] \right) \exp\left\{ -\alpha \frac{1/2 - z}{v_0} \right\}, \tag{A56}$$

where $f_t(x) = f(x, 1/2)$ and $g_t(x) = g(x, 1/2)$ are the boundary conditions at the top boundary $z = 1/2$. If we specify the boundary conditions

$$\text{at } z = 1/2, \quad \frac{\partial v_x'}{\partial x} + \frac{\partial v_z'}{\partial z} = \phi' = 0 \text{ for } x \in \mathbb{R}, \tag{A57}$$

then $f_t = g_t = 0$, which results in $\phi' = \partial v_x'/\partial x + \partial v_z'/\partial z = 0$ for $(x, z, t) \in \{\mathbb{R} \times (-1/2, 1/2) \times (0, \infty)\}$. Hence the particles initialised uniformly with concentration Φ_0 remain uniform in the domain forever in the presence of infinitesimal perturbations (Prakhar & Prosperetti 2021).

References

Abade, G.C., Grabowski, W.W. & Pawlowska, H. 2018 Broadening of cloud droplet spectra through eddy hopping: turbulent entraining parcel simulations. *J. Atmos. Sci.* **75** (10), 3365–3379.

Aleria, A., Khan, A. & Bera, P. 2024 Finite amplitude analysis of Poiseuille flow in fluid overlying porous domain. *SIAM J. Appl. Maths* **84** (2), 433–463.

Balachandar, S. & Eaton, J.K. 2010 Turbulent dispersed multiphase flow. *Annu. Rev. Fluid Mech.* **42**, 111–133.

Beard, K.V. & Ochs, H.T. III. 1993 Warm-rain initiation: an overview of microphysical mechanisms. *J. Appl. Meteorol. Climatol.* **32** (4), 608–625.

Boullé, N., Dallas, V. & Farrell, P.E. 2022 Bifurcation analysis of two-dimensional Rayleigh–Bénard convection using deflation. *Phys. Rev. E* **105** (5), 055106.

Boyd, J.P. 2001 *Chebyshev and Fourier Spectral Methods*. Courier Corporation.

Brandt, L. & Coletti, F. 2022 Particle-laden turbulence: progress and perspectives. *Annu. Rev. Fluid Mech.* **54**, 159–189.

Busse, F.H. 2003 The sequence-of-bifurcations approach towards understanding turbulent fluid flow. *Surv. Geophys.* **24**, 269–288.

Cao, W., Liu, Q., Wang, F. & Weng, C. 2024 Effects of the droplet size and engine size on two-phase kerosene/air rotating detonation engines in flight operation conditions. *Acta Astronaut.* **223**, 108–118.

Chandrakar, K.K., Saito, I., Yang, F., Cantrell, W., Gotoh, T. & Shaw, R.A. 2020 Droplet size distributions in turbulent clouds: experimental evaluation of theoretical distributions. *Q. J. R. Meteorol. Soc.* **146** (726), 483–504.

Clift, R., Grace, J.R. & Weber, M.E. 2005 *Bubbles, Drops, and Particles*. Dover.

Cross, M. & Greenside, H. 2009 *Pattern Formation and Dynamics in Nonequilibrium Systems*. Cambridge University Press.

Cross, M.C. & Hohenberg, P.C. 1993 Pattern formation outside of equilibrium. *Rev. Mod. Phys.* **65** (3), 851.

Denzel, C.J., Bragg, A.D. & Richter, D.H. 2023 Stochastic model for the residence time of solid particles in turbulent Rayleigh–Bénard flow. *Phys. Rev. Fluids* **8** (2), 024307.

Drazin, P.G. & Reid, W.H. 2004 *Hydrodynamic Stability*. Cambridge University Press.

Elperin, T., Kleeorin, N., Krasovitov, B., Kulmala, M., Liberman, M., Rogachevskii, I. & Zilitinkevich, S. 2015 Acceleration of raindrop formation due to the tangling-clustering instability in a turbulent stratified atmosphere. *Phys. Rev. E* **92** (1), 013012.

Elperin, T., Kleeorin, N., Liberman, M. & Rogachevskii, I. 2013 Tangling clustering instability for small particles in temperature stratified turbulence. *Phys. Fluids* **25** (8), 085104–085104.

Farrell, P.E., Beentjes, C.H.L. & Birkisson, A. 2016 The computation of disconnected bifurcation diagrams. *arXiv: Numerical Analysis*.

Farrell, P.E., Birkisson, A. & Funke, S.W. 2015 Deflation techniques for finding distinct solutions of nonlinear partial differential equations. *SIAM J. Sci. Comput.* **37** (4), A2026–A2045.

Gatignol, R. 1983 The faxen formulae for a rigid particle in an unsteady non-uniform stokes flow. *J. Méc. Théor. Appl.* **2** (2), 143–160. ABS 30 REF., FRE; BIBL

Gore, R.A. & Crowe, C.T. 1989 Effect of particle size on modulating turbulent intensity. *Intl J. Multiphase Flow* **15** (2), 279–285.

Grossmann, S. 2000 The onset of shear flow turbulence. *Rev. Mod. Phys.* **72** (2), 603.

Helbig, N., Vogel, B., Vogel, H. & Fiedler, F. 2004 Numerical modelling of pollen dispersion on the regional scale. *Aerobiologia* **20** (1), 3–19.

Hetsroni, G. & Sokolov, M. 1971 Distribution of mass, velocity, and intensity of turbulence in a two-phase turbulent jet. *J. Appl. Mech.* **38** (2), 315–327.

HOF, BJORN, VAN, DOORNE, C.W.H., WESTERWEEL, JERRY, NIEUWSTADT, FRANS T.M., FAISST, HOLGER, ECKHARDT, BRUNO, WEDIN, HAKAN, KERSWELL, RICHARD R. & WALEFFE, FABIAN 2004 Experimental observation of nonlinear traveling waves in turbulent pipe flow. *Science* **305** (5690), 1594–1598.

HOF, B., WESTERWEEL, J., SCHNEIDER, T.M. & ECKHARDT, B. 2006 Finite lifetime of turbulence in shear flows. *Nature* **443** (7107), 59–62.

HOYLE, R.B. 2006 *Pattern Formation: an Introduction to Methods*. Cambridge University Press.

HUANG, Z., ZHAO, M., XU, Y., LI, G. & ZHANG, H. 2021 Eulerian–Lagrangian modelling of detonative combustion in two-phase gas–droplet mixtures with OpenFOAM: validations and verifications. *Fuel* **286**, 119402.

HWANG, W. & EATON, J.K. 2006 Homogeneous and isotropic turbulence modulation by small heavy particles. *J. Fluid Mech.* **564**, 361–393.

JEFFREYS, H. 1928 Some cases of instability in fluid motion. *Proc. R. Soc. Lond. Ser. A* **118** (779), 195–208.

KHANDELWAL, M.K. & BERA, P. 2015 Weakly nonlinear stability analysis of non-isothermal Poiseuille flow in a vertical channel. *Phys. Fluids* **27** (6), 064103.

KIGER, K.T. & LASHERAS, J.C. 1997 Dissipation due to particle/turbulence interaction in a two-phase, turbulent, shear layer. *Phys. Fluids* **9** (10), 3005–3023.

KOYAGUCHI, T., HALLWORTH, M.A., HUPPERT, H.E. & STEPHEN J. SPARKS, R.S.J. 1990 Sedimentation of particles from a convecting fluid. *Nature* **343** (6257), 447–450.

KUERTEN, J.G.M. 2016 Point-particle DNS and LES of particle-laden turbulent flow-a state-of-the-art review. *Flow Turbul. Combust.* **97**, 689–713.

LANCE, M., MARIE, J.L. & BATAILLE, J. 1991 Homogeneous turbulence in bubbly flows. *J. Fluids Engng* **113** (2), 295–300.

MARTIN, D. & NOKES, R. 1988 Crystal settling in a vigorously convecting magma chamber. *Nature* **332**, 534–536.

MAXEY, M. 2017 Simulation methods for particulate flows and concentrated suspensions. *Annu. Rev. Fluid Mech.* **49** (1), 171–193.

MAXEY, M.R. & RILEY, J.J. 1983 Equation of motion for a small rigid sphere in a nonuniform flow. *Phys. Fluids* **26** (4), 883–889.

MOLER, C.B. & STEWART, G.W. 1973 An algorithm for generalized matrix eigenvalue problems. *SIAM J. Numer. Anal.* **10** (2), 241–256.

MOLINA, I., BURGISSER, A. & OPPENHEIMER, C. 2015 A model of the geochemical and physical fluctuations of the lava lake at Erebus volcano, Antarctica. *J. Volcanol. Geotherm. Res.* **308**, 142–157.

NIEMELA, J.J., SKRBEK, L., SREENIVASAN, K.R. & DONNELLY, R.J. 2000 Turbulent convection at very high Rayleigh numbers. *Nature* **404** (6780), 837–840.

ORESTA, P., FORNARELLI, F. & PROSPERETTI, A. 2014 Multiphase Rayleigh–Bénard convection. *Mech. Engng Rev.* **1** (1), FE0003–FE0003.

ORESTA, P. & PROSPERETTI, A. 2013 Effects of particle settling on Rayleigh–Bénard convection. *Phys. Rev. E* **87** (6), 063014.

PATOČKA, V., CALZAVARINI, E. & TOSI, N. 2020 Settling of inertial particles in turbulent Rayleigh–Bénard convection. *Phys. Rev. Fluids* **5** (11), 114304.

PENDAR, M.-R. & PÁSCOA, J.C. 2021 Numerical analysis of charged droplets size distribution in the electrostatic coating process: effect of different operational conditions. *Phys. Fluids* **33** (3), 033317.

POYDENOT, F. & ANDREOTTI, B. 2024 Pathways from nucleation to raindrops. *Phys. Rev. Fluids* **9** (12), 123602.

PRAKHAR, S. & PROSPERETTI, A. 2021 Linear theory of particulate Rayleigh–Bénard instability. *Phys. Rev. Fluids* **6** (8), 083901.

RAZA, S., HIRATA, S.C. & CALZAVARINI, E. 2024 Stabilization of the Rayleigh–Bénard system by injection of thermal inertial particles and bubbles. *Phys. Fluids* **36** (12), 124141.

ROBICHAUD, A. & COMTOIS, P. 2021 Numerical modelling of birch pollen dispersion in Canada. *Environ. Res.* **194**, 110554.

RUIZ, J., MACÍAS, D. & PETERS, F. 2004 Turbulence increases the average settling velocity of phytoplankton cells. *Proc. Natl Acad. Sci. USA* **101** (51), 17720–17724.

SCHLÜTER, A., LORTZ, D. & BUSSE, F. 1965 On the stability of steady finite amplitude convection. *J. Fluid Mech.* **23** (1), 129–144.

SCHWAIGER, H.F., DENLINGER, R.P. & MASTIN, L.G. 2012 Ash3d: a finite-volume, conservative numerical model for ash transport and tephra deposition. *J. Geophys. Res.: Solid Earth* **117** (B4), B04204.

SHARMA, A.K., KHANDELWAL, M.K. & BERA, P. 2018 Finite amplitude analysis of non-isothermal parallel flow in a vertical channel filled with a highly permeable porous medium. *J. Fluid Mech.* **857**, 469–507.

SHAW, R.A. 2003 Particle–turbulence interactions in atmospheric clouds. *Annu. Rev. Fluid Mech.* **35** (1), 183–227.

SHUKLA, P. & ALAM, M. 2011 Weakly nonlinear theory of shear-banding instability in a granular plane Couette flow: analytical solution, comparison with numerics and bifurcation. *J. Fluid Mech.* **666**, 204–253.

SQUIRES, K.D. & YAMAZAKI, H. 1995 Preferential concentration of marine particles in isotropic turbulence. *Deep-Sea Res. I: Oceanogr. Res. Papers* **42** (11–12), 1989–2004.

SRINIVAS, T. & TOMAR, G. 2024 Particle cloud patterns in Rayleigh–Bénard convection. In *Proceedings of the 27th National and 5th International ISHMT-ASTFE Heat and Mass Transfer Conference December 14–17 2023*. IIT Patna, Begel House Inc.

SRINIVAS, T. & TOMAR, G. 2025 A generalized correction scheme for two-way coupled particle-laden Euler–Lagrange simulations. *Comput. Fluids* **290**, 106554.

STEWARTSON, K. & STUART, J.T. 1971 A non-linear instability theory for a wave system in plane Poiseuille flow. *J. Fluid Mech.* **48** (3), 529–545.

STUART, J.T. 1960 On the non-linear mechanics of wave disturbances in stable and unstable parallel flows. Part 1. The basic behaviour in plane Poiseuille flow. *J. Fluid Mech.* **9** (3), 353–370.

SUN, T.Y. & FAETH, G.M. 1986 Structure of turbulent bubbly jets – I. Methods and centerline properties. *Intl J. Multiphase Flow* **12** (1), 99–114.

WEIDEMAN, J.A. & REDDY, S.C. 2000 A MATLAB differentiation matrix suite. *ACM Trans. Math. Softw.* **26** (4), 465–519.

YAO, L.S. & ROGERS, B.B. 1992 Finite-amplitude instability of non-isothermal flow in a vertical annulus. *Proc. R. Soc. Lond. Ser. A: Math. Phys. Sci.* **437** (1900), 267–290.

YARUSHINA, V.M., BERCOVICI, D. & MICHAUT, C. 2015 Two-phase dynamics of volcanic eruptions: particle size distribution and the conditions for choking. *J. Geophys. Res.: Solid Earth* **120** (3), 1503–1522.

ZHONG, J.-Q., FUNFSCHILLING, D. & AHLERS, G. 2009 Enhanced heat transport by turbulent two-phase Rayleigh–Bénard convection. *Phys. Rev. Lett.* **102** (12), 124501.